

Many-body Physics of Ultracold Alkaline-Earth atoms with $SU(N)$ -symmetric interactions

Eduardo Ibarra-García-Padilla^{1,2}, Sayan Choudhury³

¹ Department of Physics and Astronomy, University of California, Davis, CA 95616, USA

² Department of Physics and Astronomy, San José State University, San José, California 95192, USA

³ Harish-Chandra Research Institute, a CI of Homi Bhabha National Institute, Chhatnag Road, Jhunsi, Allahabad 211019

E-mail: edibarra@ucdavis.edu, sayanchoudhury@hri.res.in

Abstract. Symmetries play a crucial role in understanding phases of matter and the transitions between them. Theoretical investigations of quantum models with $SU(N)$ symmetry have provided important insights into many-body phenomena. However, these models have generally remained a theoretical idealization, since it is very difficult to exactly realize the $SU(N)$ symmetry in conventional quantum materials for large N . Intriguingly however, in recent years, ultracold alkaline-earth-atom (AEA) quantum simulators have paved the path to realize $SU(N)$ -symmetric many-body models, where N is tunable and can be as large as 10. This symmetry emerges due to the closed shell structure of AEAs, thereby leading to a perfect decoupling of the electronic degrees of freedom from the nuclear spin. In this work, we provide a systematic review of recent theoretical and experimental work on the many-body physics of these systems. We first discuss the thermodynamic properties and collective modes of trapped Fermi gases, highlighting the enhanced interaction effects that appear as N increases. We then discuss the properties of the $SU(N)$ Fermi-Hubbard model, focusing on some of the major experimental achievements in this area. We conclude with a compendium highlighting some of the significant theoretical progress on $SU(N)$ lattice models and a discussion of some exciting directions for future research.

Keywords: $SU(N)$ many-body models, quantum simulation, ultracold alkaline-earth atoms

1. Introduction

Rapid advances in the development of ultracold atomic systems have provided physicists with a powerful platform to explore various facets of many-body physics [1]. In particular, ultracold atoms loaded in optical lattices provide a versatile platform for the quantum simulation of both equilibrium and non-equilibrium physics [2, 3]. These systems provide unprecedented control over the effective lattice geometries as well as the strength and range of the inter-atomic interactions, thereby providing a pathway to address unresolved questions about emergent phenomena [4–7]. Furthermore, these systems can be employed to synthesize new forms of quantum matter that go beyond the capabilities of conventional quantum materials and can be harnessed for quantum information processing tasks [8–10].

Most initial experimental efforts in this area focused on trapping and cooling alkali atoms [11, 12]. These atoms have only one valence electron thereby enabling the application of several quantum control techniques. Furthermore, in certain atomic species such as ^6Li or ^{40}K , the scattering length can be tuned by employing magnetic Feshbach resonances, thereby providing a knob to control the strength of the interactions [13]. However, the range of phenomena that can be investigated using alkali atoms is somewhat limited due to their atomic structure. A promising avenue to go beyond the limitations of alkali gases has been provided by Alkaline-Earth-like atoms (AEAs). AEAs are the elements that belong to group II of the periodic table (Be, Mg, C, Sr, Ba, and Ra), but also the rare-earth element Yb. These elements are characterized by full inner shells and two outer valence electrons in a filled s-shell. Due to their filled inner shells, the two valence electrons govern most of these atoms' chemical and electronic properties. Most experiments with AEAs in have employed ^{173}Yb ($I = 5/2$) and ^{87}Sr ($I = 9/2$); or concreteness, we will discuss the electronic structure of Yb in detail in the next sub-section, but the ideas are applicable also for Sr.

1.1. Electronic structure of AEAs

The electronic configuration of ^{173}Yb is $[\text{Xe}]4\text{f}^{14}6\text{s}^2$. It has filled f- and s-shells. Yb exhibits an electronic structure with spin-singlet ($S = 0$) and spin-triplet ($S = 1$) manifolds. To a first approximation, its level structure is well described in the LS-coupling scheme, where coupling between the total orbital angular momentum \mathbf{L} and the total spin of the valence electrons \mathbf{S} gives the total electronic angular momentum $\mathbf{J} = \mathbf{L} + \mathbf{S}$, and eigenstates are labelled as $^{2S+1}L_J$. Fig. 1 displays the level structure for ^{173}Yb with the most significant optical transitions. The ground state of ^{173}Yb is a spin singlet 1S_0 with $J = 0$; it also exhibits two metastable states, the 3P_0 state and the 3P_2 state. In particular, the 3P_0 state has a lifetime $\tau \approx 20$ seconds, and also has no total electronic angular momentum ($J = 0$) like the ground state 1S_0 . This has far-reaching implications on the properties of the states, since in this case:

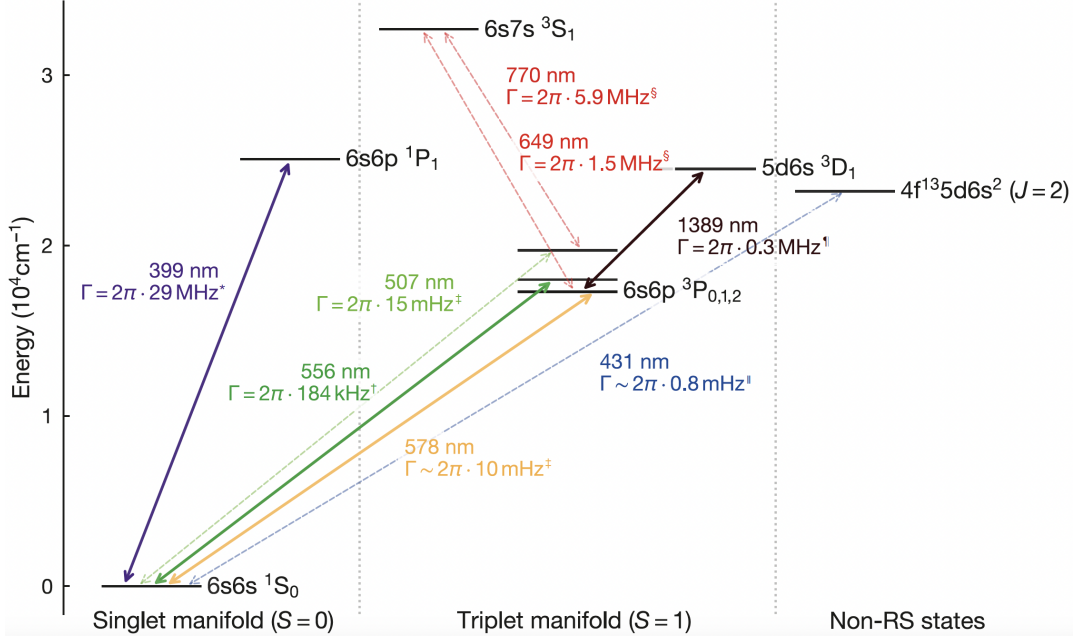


Figure 1. Partial electronic structure of ytterbium. The states are labelled according to the Russell-Saunders (RS) notation when the f-shell is closed and in terms of total angular momentum J when the f-shell is open. The wavelength λ and the linewidth Γ are specified for each transition. References for the values of the linewidths: * [14], † [15], ‡ [16], § [17], ¶ [18], ¹ [19, 20]. Figure and caption reprinted with copyright permission of Ref. [21].

- The total angular momentum of the atom \mathbf{F} is given only by the nuclear spin \mathbf{I} ($\mathbf{F}=\mathbf{I}$). The $SU(N)$ symmetric nature of interactions for the fermionic isotopes results from this decoupling of the nuclear spin degree of freedom from the electronic structure, as we will discuss in the following section \ddagger .
- The state does not exhibit a hyperfine structure, since $\mathbf{I} \cdot \mathbf{J} = 0$, and therefore is almost completely insensitive to magnetic fields because fermionic and bosonic isotopes have a weak or zero nuclear magnetic moment, respectively \S . This insensitivity has relevant consequences in how interactions can be tuned for ^{173}Yb atoms, since magnetic Feshbach resonances, which are typically employed to control the s-wave scattering length between two hyperfine states in alkali-atoms [22], are experimentally unavailable due to the requirement for extremely high magnetic fields that are not achievable in laboratories. There are, however, optical Feshbach resonances that can be used to tune interactions between different m_I states. These have been used by several groups to realize Optical Stern Gerlach measurements and/or break the $SU(N)$ symmetric interactions [23–25].

\ddagger Yb has fermionic isotopes ^{171}Yb and ^{173}Yb , which possess a nuclear spin $I = 1/2$ and $I = 5/2$, respectively; and bosonic isotopes ^{168}Yb , ^{170}Yb , ^{172}Yb , ^{174}Yb , and ^{176}Yb , all of which have $I = 0$.

\S For fermions, the only magnetic moment arises from the nuclear spin, which is essentially irrelevant since the nuclear magneton μ_N is approximately 2000 times smaller than the Bohr magneton μ_B of the electron.

1.2. $SU(N)$ -symmetric interactions

Since $J = 0$, the ground state 1S_0 and the metastable state 3P_0 exhibit perfect decoupling of the nuclear spin from the electronic structure due to the lack of hyperfine structure. In these states, the spin is protected inside the nucleus and it is not affected by the physics occurring at the electronic cloud distance scales. This has an important effect on the properties of atomic collisions because, aside from Pauli exclusion, nuclei can only affect collisions through hyperfine coupling to the electron angular momentum \parallel . In dilute atomic gases at low-temperatures, scattering properties are well characterized by the s -wave scattering length. For fermionic gases with $N = 2I + 1$ spin components is possible to model the collisions with the following pseudo-potential [27],

$$V(\mathbf{r}) = \frac{4\pi\hbar^2}{m} \sum_{F_t=0,2,\dots}^{N-2} a_{F_t} \delta(\mathbf{r}) \mathcal{P}_{F_t}, \quad (1)$$

where \hbar is the reduced Planck's constant, m is the mass of the colliding atoms, \mathcal{P}_{F_t} is the projector on states with even total spin $F_t = 0, 2, 4, \dots, N - 2$ of the atom pair, and a_{F_t} is the scattering length for a given F_t ¶.

For the two-body collision of atoms in states $|F, m_1\rangle$, $|F, m_2\rangle$ and total spin $|F_t, m_t = m_1 + m_2\rangle$, the initial state $|F, m_1\rangle|F, m_2\rangle$ will couple to a different spin combination $|F, m_3\rangle|F, m_4\rangle$ via the pseudo-potential in eq. (1),

$$\langle F, m_4; F, m_3 | V(\mathbf{r}) | F, m_1; F, m_2 \rangle = \frac{4\pi\hbar^2}{m} \delta(\mathbf{r}) \sum_{F_t=0,2,\dots}^{N-2} \sum_{m_t=-F_t}^{F_t} a_{F_t} C_{Fm_1 Fm_2}^{F_t m_t} C_{Fm_3 Fm_4}^{F_t m_t}. \quad (2)$$

where $C_{j_1 m_1 j_2 m_2}^{JM}$ are the Clebsh-Gordan coefficients and we used that $\mathcal{P}_{F_t} = \sum_{m_t=-F_t}^{F_t} |F_t, m_t\rangle\langle F_t, m_t|$. Eq. (2) reflects that momentum conservation ensures that the total spin F_t and its projection m_t are conserved during the collision ($m_t = m_1 + m_2 = m_3 + m_4$), but the spin projection of the individual atoms is not.

In the case of AEAs, the scattering lengths are equal for all possible F_t pairs ($a_{F_t} = a \forall F_t$), since the nuclear spin is decoupled from the electronic structure, and therefore its influence in the scattering process is simply reduced to Pauli exclusion principle. Because of the orthogonality relationships of the Clebsch-Gordan coefficients $\sum_J \sum_M C_{j_1 m_2 j_2 m_2}^{JM} C_{j_1 m_1, j_2 m_2'}^{JM} = \delta_{m_1, m_1'} \delta_{m_2, m_2'}$ one observes that in contrast to the general case of collisions, for AEAs the spin projection m_F of each colliding atom is preserved and thus spin relaxation to other m_F states is forbidden. This means that the interaction will be $SU(N)$ symmetric, and the interaction pseudopotential

|| Magnetic dipole-dipole interactions between the nuclear spin of two atoms is negligible in comparison to the induced dipole-dipole interactions of the electronic clouds [26].

¶ Only states with even total spin F_t can contribute to the scattering process because of the antisymmetrization of the wavefunction. In s -wave scattering collisions the spatial wave function is symmetric, and therefore the spin wave function has to be antisymmetric.

simplifies to $V(\mathbf{r}) = (4\pi\hbar^2/m)a\delta(\mathbf{r})$ for all possible pairs of spin projections. Ref. [26] provides theoretical estimates for the $SU(N)$ symmetry breaking of AEAs. The variation in the scattering length for different nuclear spins in the ground state 1S_0 is of the order $\delta a_{gg}/a_{gg} \sim 10^{-9}$, while for the excited metastable state 3P_0 these are of order $\delta a_{ee}/a_{ee} \sim \delta a_{eg}^\pm/a_{eg}^\pm \sim 10^{-3}$ ⁺ (here the perfect decoupling is slightly broken by the admixture with higher-lying P states with $J \neq 0$).

1.3. Structure of the review

Now that we have introduced the electronic structure of AEA gases and demonstrated that they exhibit an emergent $SU(N)$ symmetry, we will proceed to review the many-body physics of these systems. This review is organized as follows. In sec. 2, we discuss some interesting theoretical advancements and experimental results on trapped $SU(N)$ Fermi gases. In sec. 3, we discuss some of the major works on quantum simulation of the $SU(N)$ Fermi-Hubbard model with ultracold AEAs in optical lattices. While we primarily focus on experimental achievements, we also provide a compendium of theoretical works on $SU(N)$ lattice models such as the Hubbard model, the Heisenberg model, and the $t - J$ model. Furthermore, we note that while lattice AEA systems provide a powerful platform for precision timekeeping and quantum computing, we do not delve into these aspects in this review. We conclude in sec. 4 by outlining some interesting directions for future research.

2. Many-body physics of Trapped AEA Gases

The enlarged $SU(N)$ symmetry results in enhanced interaction effects in trapped AEA gases. This has remarkable consequences such as a strong N -dependence of the compressibility and collective mode frequencies as well as bosonization in higher dimensions. We now proceed to expand on these developments.

2.1. Thermodynamics of the $SU(N)$ Fermi Liquid

We begin by examining the extension of the Fermi liquid theory for N -component fermions with $SU(N)$ symmetric interactions; this system is described by:

$$H = \sum_{\mathbf{k},\gamma} \left(\frac{k^2}{2m} - \mu \right) c_{\mathbf{k},\gamma}^\dagger c_{\mathbf{k},\gamma} + \frac{g}{2} \sum_{\mathbf{k}_1, \mathbf{k}_2, \mathbf{k}_3, \mathbf{k}_4, \gamma_1 \neq \gamma_2} c_{\mathbf{k}_1, \gamma_1}^\dagger c_{\mathbf{k}_2, \gamma_2}^\dagger c_{\mathbf{k}_3, \gamma_1} c_{\mathbf{k}_4, \gamma_2} \delta_{\mathbf{k}_1 + \mathbf{k}_2, \mathbf{k}_3 + \mathbf{k}_4}, \quad (3)$$

⁺ Scattering processes between two atoms in the ground state are denoted by a_{gg} , two atoms in the excited state by a_{ee} , and one atom in the excited state and the other one in the ground state in their triplet (+) or singlet (-) configuration by a_{eg}^\pm .

where $c_{\mathbf{k},\gamma}$ is the annihilation operator for a fermion of species γ and momentum \mathbf{k} . The standard Fermi Liquid (FL) theory was formulated for a two-component fermionic system with $SU(2)$ symmetry. This theory was generalized to the $SU(N)$ scenario by Yip, Huang, and Kao [28] (see Ref. [29] and Ref. [30] for extensions to finite temperatures and one-dimension respectively). They did this by describing the change in the quasi-particle energy at \mathbf{k} , $\delta\epsilon_{\alpha\beta}(\mathbf{k})$ as a $N \times N$ matrix, that is related to the low-energy quasi-particle excitations, $\delta n_{\delta\gamma}$ by:

$$\delta\epsilon_{\alpha\beta}(\mathbf{k}) = \sum_{\mathbf{k}',\gamma,\delta} f_{\alpha\gamma,\beta\delta}(\mathbf{k}, \mathbf{k}') \delta n_{\delta\gamma}(\mathbf{k}'), \quad (4)$$

where

$$f_{\alpha\gamma,\beta\delta}(\mathbf{k}, \mathbf{k}') = f_s(\mathbf{k}, \mathbf{k}') \delta_{\alpha\beta} \delta_{\gamma\delta} + 4f_m(\mathbf{k}, \mathbf{k}') \sum_a T_{\alpha\beta}^a T_{\gamma\delta}^a, \quad (5)$$

where the matrices T^a are the generators of the $SU(N)$ group. It is now fairly straightforward to extend the results for Landau FL theory for $SU(N)$ fermions. There are some remarkable consequences of this generalization. For instance, the Stoner instability in the $SU(2)$ FL leads to a continuous phase transition from the paramagnetic to the Ferromagnetic phase. However, for $N > 2$, this transition can become discontinuous [31–33]. Another important quantity that is strongly influenced by N is the isothermal compressibility, $\kappa = \frac{1}{n^2} \frac{dn}{d\mu}$ given by

$$\frac{\kappa_0}{\kappa} = 1 + (N-1) \frac{2k_F a}{\pi} \left[1 + \frac{2k_F a}{15\pi} (22 - 4 \ln 2) \right]. \quad (6)$$

where κ_0 is the compressibility when $a = 0$, n is the particle density, and μ is the chemical potential. Thus, in the weakly interacting regime ($k_F a \ll 1$), the $SU(N)$ gas is effectively $(N-1)$ -fold more repulsive than the $SU(2)$ -gas.

Sonderhouse *et al.* measured this compressibility experimentally by examining the local density fluctuations [34]. Employing the fluctuation-dissipation theorem, the relative number fluctuations, η of a small sub-region of the gas having an average of \bar{N}_s atoms can be related to κ as $\eta = \Delta \bar{N}_s^2 / \bar{N}_s = n k_B T \kappa$. To the first order in both temperature and the scattering length, a , one obtains:

$$\eta = \frac{3}{2} \frac{T/T_F}{1 + \frac{2}{\pi} (k_F a) (N-1)}, \quad (7)$$

which clearly shows the enhanced effect of the repulsive interaction. We note that this expression can also be obtained by a virial expansion of the partition function. From their measurements, the authors find that $T/T_F = 0.16 \pm 0.01$, thereby indicating that the gas is in the deeply degenerate regime. However, it is interesting to note that the effect of interactions on the density fluctuations can also be mimicked by lowering the temperature of a non-interacting gas. Thus, to better characterize the interaction effects, the experimentalists also investigated the dynamics of the gas after being released from

the trap. In the expansion dynamics, the interactions lead to a preferential movement of the atoms in the direction of the largest density gradient lead to an anisotropic distribution of the cloud after sufficiently long-times. The experimental results are shown in Fig. 2; the strong role of interactions is evident here.

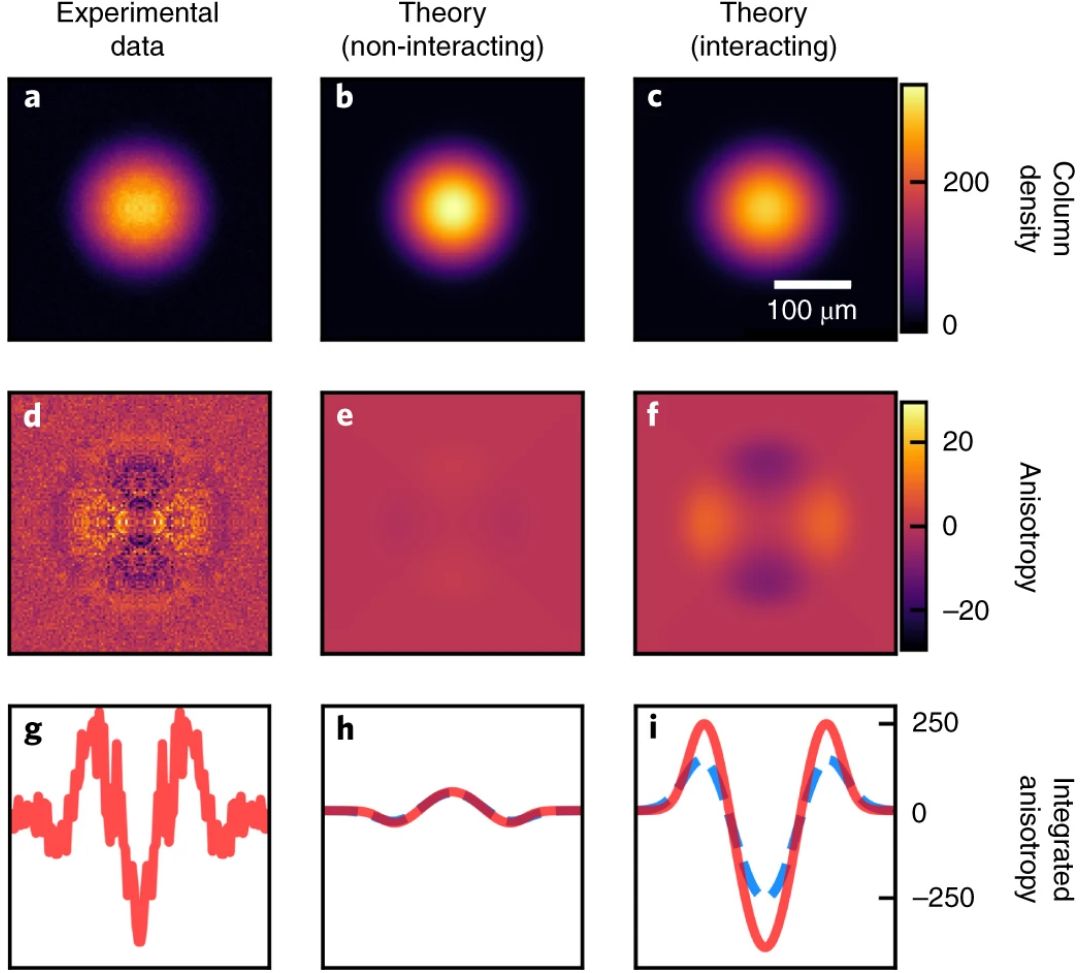


Figure 2. (a)-(c) shows the integrated atomic density obtained after time-of-flight. The anisotropy of the cloud shown in (d)-(f) reflects the anisotropy of the trap. (g)-(i) shows the anisotropy integrated along one direction. The red lines shows the anisotropy of the images in (d)-(f), while the dashed blue lines correspond to the anisotropy obtained using a higher temperature. Figure reprinted with copyright permission of Ref. [34].

2.2. Bosonization and Collective Modes

One of the most intriguing features of a N -component Fermi gas is that this system would exhibit bosonic behavior in the large- N limit. This bosonization arises from a weakened impact of the Pauli exclusion principle due to the large number of internal states and is well-established in one-dimensional systems. In 2012, the Florence

group demonstrated this one-dimensional bosonization in Ref. [35]. Intriguingly, recent theoretical results and experimental investigations have provided strong evidence for bosonization in higher dimensions. This has been achieved by probing the N -dependence of the collective mode frequencies and the contact in these systems. We now proceed to describe these studies.

The collective oscillations of trapped quantum gases in response to external perturbations provide important insights into the many-body physics of these systems. These oscillations have been extensively studied in the case of two-component Fermi gases, where the collective mode frequencies and their damping rates reveal the effects of interactions. He *et al.* have extended these studies to the case of AEA by examining the breathing and quadrupole modes of a two-dimensional Fermi gas of ^{173}Yb ; they performed the experiment by suddenly increasing the radial trap frequency, thereby exciting multiple collective modes [36]. The frequency of each collective mode was separately extracted by tracking the center-of-mass and the cloud width. The results obtained are shown in Fig. 3(a). It is clear that the breathing mode does not show any dependence on the spin multiplicity and stays at the value of $2\omega_d$, where ω_d is the dipole mode frequency; this is a consequence of classical scale invariance in a weakly interacting two-dimensional gas. In contrast, mean-field effects lead to a clear dependence of the quadrupole mode frequency, $\omega_q \propto (2\omega_d - g_{2D}(N-1))$. We note that these experiments were performed in the ‘collisionless’ regime. In contrast, in the hydrodynamic regime, collisions become extremely important. In this case, the quadrupole-mode frequency is N -independent $\omega_q^{\text{hd}} = \sqrt[2]{\omega_d}$. Finally, we note that the damping rate of these oscillations, $\frac{1}{\tau} \propto (N-1)$, thereby highlighting the enhanced effect of the interactions [37].

While collective modes play an important role in characterizing the many-body physics of Fermi gases, the thermodynamic properties of a dilute quantum gas can be captured succinctly by the contact, C [39–41]. In particular, C governs various thermodynamic quantities via universal relations. In Ref. [38], Song *et al.* measured the N -dependence of s-wave contact C from the momentum distribution of the fermi gas. Due to the spin-independent nature of the interactions, the large-momentum tail scales as $n(\mathbf{k}) = C_0/|\mathbf{k}|^4$, where $C_{SU(N)} = c_{\text{pair}}N_{\text{tot}}^2(1 - 1/N)$, where N_{tot} is the total number of fermions. Interestingly, the large-momentum tail for spinless bosons is given by $C_B = c_{\text{pair}}N_{\text{tot}}(N_{\text{tot}} - 1) \approx c_{\text{pair}}N_{\text{tot}}^2$. Thus $C_{SU(N)}$ approaches C_B with a $1/N$ scaling thereby demonstrating bosonization in three dimensions.

3. Quantum simulation with ultracold AEAs in optical lattices

Quantum simulation with ultracold atoms in optical lattices (OLs) has provided with an unparalleled avenue to study many-body Hamiltonians relevant to condensed matter physics [42–45]. One the primary directions of the field is the experimental study of the Fermi-Hubbard model (FHM) [46–49]. The FHM model is central to

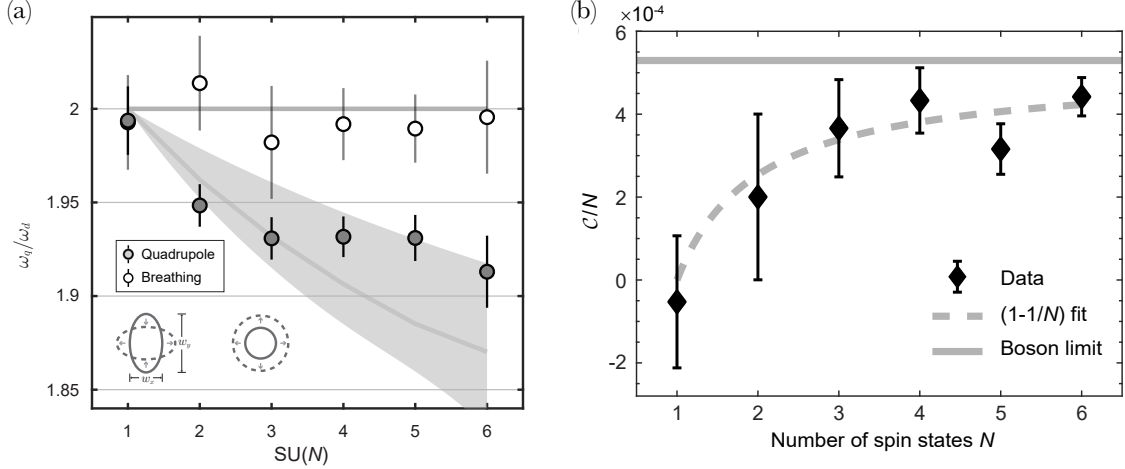


Figure 3. (a) The N –dependence of the breathing and quadrupole mode frequencies of a trapped gas of ^{173}Yb atoms in two dimensions. The breathing mode does not show any N –dependence due to a classical scale invariance, while the quadrupole modes show a strong N –dependence. Figure reprinted and modified with permission from Ref. [36]. (b) The s-wave contact C of $\text{Su}(N)$ fermions shows a strong N –dependence approaching the bosonic value, C_B as N increases ($C_{\text{SU}(N)} \sim C_B(1-1/N)$). This shows the weakened effect of the Pauli exclusion principle. Figure reprinted and modified with permission from Ref. [38].

condensed matter physics since it is one of the simplest models that captures the essential features of strongly correlated materials and because it accounts for many canonical correlated phases of matter these systems exhibit. For example, in the two-dimensional (2D) square lattice, it displays many of the phenomena observed in strongly correlated materials such as the Mott insulating phase, long-range antiferromagnetic order, superconductivity, charge density waves, and it is frequently studied in the context of d -wave superconductivity [50–55].

In its original $\text{SU}(2)$ symmetric form, the Fermi Hubbard Model (FHM) describes the dynamics of spin-1/2 particles on a lattice with a nearest-neighbor tunneling amplitude t , and an on-site interaction U :

$$H = -t \sum_{\sigma=\uparrow,\downarrow} \left[\sum_{\langle i,j \rangle} (c_{i\sigma}^\dagger c_{j\sigma} + \text{h.c.}) - \mu \sum_i n_{i\sigma} \right] + U \sum_i n_{i\uparrow} n_{i\downarrow}, \quad (8)$$

where $\langle i,j \rangle$ denotes nearest neighbors, $c_{i\sigma}^\dagger$ ($c_{i\sigma}$) is the creation (annihilation) operator for a fermion with spin σ on-site i , $n_{i\sigma} = c_{i\sigma}^\dagger c_{i\sigma}$ is the number operator for spin σ on site i , and μ is the chemical potential that controls the fermion density. The FHM successfully captures the physics of alkali atoms loaded in OLs. In these experiments, different hyperfine states of the alkali atom are used to represent the possible spin projections $\pm 1/2$. The density is set by controlling the number of particles N_\uparrow and N_\downarrow loaded into the lattice. The tunneling rate t is controlled by changing the lattice depth, and the interaction strength U is tuned via a magnetic Feshbach resonance. For further details,

Refs. [42–44] provide a comprehensive review of the capabilities of these quantum simulators and their experimental tools.

In the case of fermionic alkaline-earth-like atoms (AEAs) in their ground state, by selective populating nuclear spin projection states m_I and loading them into an OL, experiments can engineer the $SU(N)$ FHM with tunable N from $2, \dots, 10$. The $SU(N)$ Hamiltonian is,

$$H = -t \sum_{\sigma} \left[\sum_{\langle i,j \rangle} \left(c_{i\sigma}^{\dagger} c_{j\sigma} + \text{h.c.} \right) - \mu \sum_i n_{i\sigma} \right] + \frac{U}{2} \sum_{i,\sigma \neq \tau} n_{i\sigma} n_{i\tau}, \quad (9)$$

where $\sigma = 1, \dots, N$ are the spin flavors, and $N = 2I + 1$, where I is the nuclear spin of the atoms. The Hamiltonian is graphically depicted in Fig. 4 *. Analogous to the $SU(2)$ FHM, the Hamiltonian in Eq. (9) exhibits a $U(1)$ symmetry which is reflective of a global charge conservation, i.e. the total number of particles is conserved, $[H, \sum_{i\sigma} n_{i\sigma}] = 0$. In addition, the Hamiltonian is $SU(N)$ symmetric, since the energy scales t, U, μ are independent from σ . Experimentally, this means that (1) since t and μ are controlled in a similar fashion to the alkali case, balanced mixtures of N_{σ} atoms can be loaded into a lattice with a desired depth which is independent of the spin flavor. (2) The spin independence of the interaction term, i.e. $U_{\sigma,\tau} = U \forall \sigma, \tau$ arises from the fact that fermionic AEAs feature an almost perfect decoupling of the nuclear spin I from the electronic structure in the ground state. Because of this decoupling, the s-wave scattering lengths a for different m_I exhibit predicted variations of the order of 10^{-9} [26, 61, 62], and therefore the interaction strength U (which is proportional to a) is independent of σ .

Mathematically, the $SU(N)$ symmetry of Eq. (9) means that the generators of the group, which are linear combinations of the spin permutation operators $S_{\sigma}^{\tau} = \sum_i c_{i\tau}^{\dagger} c_{j\sigma}$, satisfy the $SU(N)$ algebra $[S_{\sigma}^{\tau}, S_{\alpha}^{\beta}] = \delta_{\alpha\tau} S_{\sigma}^{\beta} - \delta_{\sigma\beta} S_{\alpha}^{\tau}$, and commute with the Hamiltonian $[H, S_{\sigma}^{\tau}] \forall \sigma, \tau$. The $SU(N)$ symmetry is reflective of the spin isotropy, and similarly to the $SU(2)$ case, the individual spin populations are conserved, since $S_{\sigma}^{\sigma} = \sum_i n_{i\sigma}$ commutes with H . For further details on $SU(N)$ group theory, ref. [61] provides a useful brief digest, and ref. [64] is a comprehensive resource for group theory in general.

Before we proceed to discuss the study of the $SU(N)$ FHM using AEAs in OLs, a few important remarks are important to discuss:

* The interest in $SU(N)$ symmetric Hamiltonians is not limited to Hubbard and Heisenberg models, but also in two-band models such as the $SU(N)$ Kondo Lattice Model (KLM) [56, 57] which is commonly used in the study of manganese oxide perovskites [58] and heavy-fermion materials [59]. However, as of today, experimental efforts have mostly studied the single-band $SU(N)$ Hubbard model, and we will therefore focus our attention on this model in this review. Further discussion in how the $SU(N)$ KLM can be engineered with AEAs in OLs is presented in Refs. [26, 60].

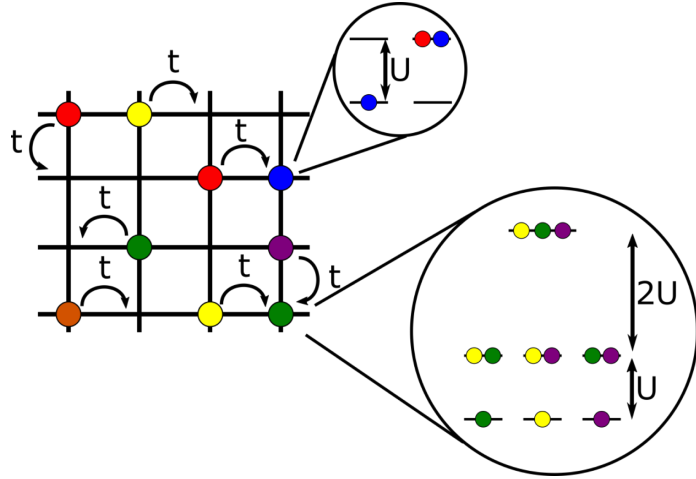


Figure 4. In the $SU(N)$ Fermi Hubbard model, particles with spin flavor $\sigma = 1, \dots, N$ (denoted by different colors) live on a lattice. These particles can tunnel to neighboring sites with a hopping amplitude t . When m atoms of different color occupy the same site, the energy is raised by Um . The filling fraction is controlled by a uniform chemical potential μ (not depicted here). Figure reprinted with copyright permission of Ref. [63].

(i) **Quantum fluctuations are important in the $SU(N)$ FHM.**

A common question we have encountered arises in terms of the $1/N$ expansion, and the assumption is that since the spin has been enlarged, the system should behave more classically. However, that is not the case.

The $1/N$ expansion technique was first used to understand spin-1/2 systems that exhibit $SU(2)$ spin symmetry. In this expansion, one reduces the role of quantum fluctuations by considering the classical limit of magnets with large spin S . In doing so, the expectation value of the spins acquires a definite value with a small variation around this saddle point and thus the $1/N$ expansion provides a method to therefore obtain mean field theories [65–69].

In the $1/N$ expansion, the relevant operators are the raising and lowering operators S^\pm , which only connect two possible values of the spin projections $\pm 1/2$, and therefore as S increases, the variance of the spin projection falls off as $1/S$. In contrast, for the $SU(N)$ case even though $1/N$ can be small, the spin permutation operators S_σ^τ connect all possible values of the spin projection and therefore quantum fluctuations are relevant and play a major role in the ground state spin structure (see Fig. 5). For this reason, in the $SU(N)$ case the variance does not go like $1/N$.

(ii) **The $SU(N)$ FHM is a limit of multi orbitals models.**

Another common question is related to the connection to solid state systems. In particular, that if electrons are spin-1/2 particles, what do the spin flavors mean in the $SU(N)$ FHM.

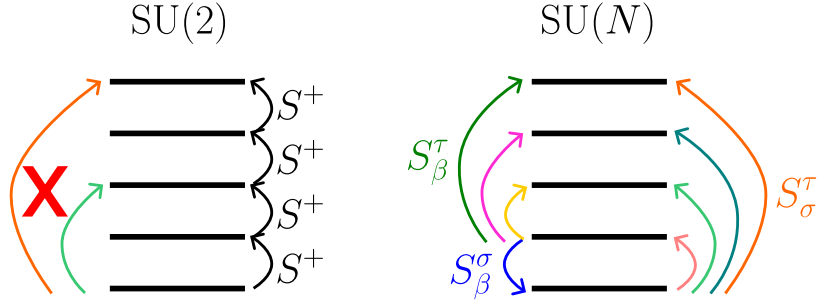


Figure 5. In the $1/N$ expansion, the underlying algebra is $SU(2)$, and different states can only be reached by subsequent applications of the raising and lowering operators (S^+ depicted in the image). On the contrary for the $SU(N)$ algebra, the spin permutation operators S_σ^τ connect all possible states. While in the former one the variance of the spin expectation value decreases with the number of states, in the latter one quantum fluctuations play an important role in the physics.

In our introduction of the $SU(N)$ FHM we mentioned we have N spin flavors, which in the context of quantum simulation with AEAs correspond to the nuclear spin projections m_I . In order to make the connection with the problem of electrons in a solid, we need to recall that an electron that is bound to or nearly localized on a specific site has three attributes: charge, spin, and orbital. While the $SU(2)$ FHM considers a single orbital and the spin degree of freedom which is invariant under $SU(2)$ rotations, multi orbital models correspond to models in which higher orbitals are now considered.

The $SU(N)$ FHM is a limit of multi orbitals models, such as the ones used to describe transition metal oxides [70–72], in which the Hubbard parameters are independent of the spin and orbital degrees of freedom. It is worth noting that such enhanced symmetry is a crude approximation in solid state systems, where interactions between different orbitals may vary over 10% or more [71]. On the other hand, for ultracold atomic experiments the $SU(N)$ symmetry holds down to many orders of magnitude as previously discussed.

We now proceed to discuss the ground-breaking experimental achievements in quantum simulators using ultracold ^{173}Yb OLs. For organizational purposes we separate these into two categories: (1) measurements of the equations of state, in which characterization of the $SU(N)$ FHM thermodynamic variables are explored and (2) quantum magnetism, in which the emphasis is focused on measuring spin correlation functions. We note that even without interactions, the spin states of AEA atoms can be employed to realize synthetic dimensions. In particular, the Florence group has realized synthetic hall ribbons with ^{173}Yb atoms and observed topological edge states [73]. However, in this work, we primarily focus on studies, where interactions play a crucial role.

3.1. Equations of state of $SU(N)$ FHM

In this sub-section, we review some of the key experiments that investigated the equations of state of the $SU(N)$ -FHM.

3.1.1. $SU(6)$ Mott Insulator

In a pioneering experiment in 2012, the Kyoto group successfully achieved the realization of an $SU(6)$ -symmetric Mott insulator in a three-dimensional (3D) optical lattice [74]. The importance of this study is three-fold: Firstly, this provided an experimental realization of an $SU(N > 2)$ Fermi Hubbard model. Secondly, it provided experimental evidence of a robust Mott plateau and the opening of charge gap via the demonstration of a suppression in the isothermal compressibility for $N = 6$. Thirdly, it demonstrated a process analogous to “Pomeranchuk” cooling in solid ${}^3\text{He}$.

In this experiment, the $SU(N)$ Fermi Hubbard model was realized by loading a balanced mixture of all the possible nuclear projections of ${}^{173}\text{Yb}$ in its ground state in a three dimensional cubic optical lattice. The experiment started with a balanced mixture of all nuclear spin states which is evaporatively cooled in a crossed far-off resonant optical trap. At the end of evaporation, the experimentalists had $1 - 3 \times 10^4$ atoms with a temperature $\sim 0.2T_F$. Atoms were subsequently loaded into an optical lattice with lattice constant $d = 266$ nm. The lattice depth was varied from 6-13 E_R , to achieve $U/6t \in [1.8, 18.6]$.

Figs. 6 and 7 summarize the main results of this experiment. In Fig. 6, the authors present experimental evidence of the charge gap in the $SU(6)$ Mott insulator by performing lattice modulation spectroscopy [75]. In this technique, resonant tunneling to the occupied sites at the modulation frequency close to the Mott gap U is obtained by periodically modulating the lattice depth. This kind of tunneling induces double occupancies, which can then be measured using the photoasociation technique [76, 77]. The Mott gaps are clearly observed in Fig. 6 at higher lattice depths.

In Fig. 7, the authors present experimental evidence of “Pomeranchuk” cooling for $N = 6$. Pomeranchuk cooling is a process by which the entropy from the motional degrees of freedom is absorbed by the large spin, leading to lower temperatures. This cooling is reflected in the final temperature of the sample, and it was observed by comparing results for $N = 2$ and $N = 6$, for which the final temperature in the lattice after adiabatic loading (i.e. total number of particles and entropy are conserved) is lower for $N = 6$ than for $N = 2$ (see Fig. 7b). As stated earlier, the lower temperature for larger N is a consequence of the different entropy an isolated spin can carry, which is $\propto \ln(N)$. In addition, Fig. 7c demonstrates that for the lowest temperature T/t achieved in each case, only the $N = 6$ case develops a robust Mott plateau at the center of the trap with an entropy per site close to $\ln(N)$.

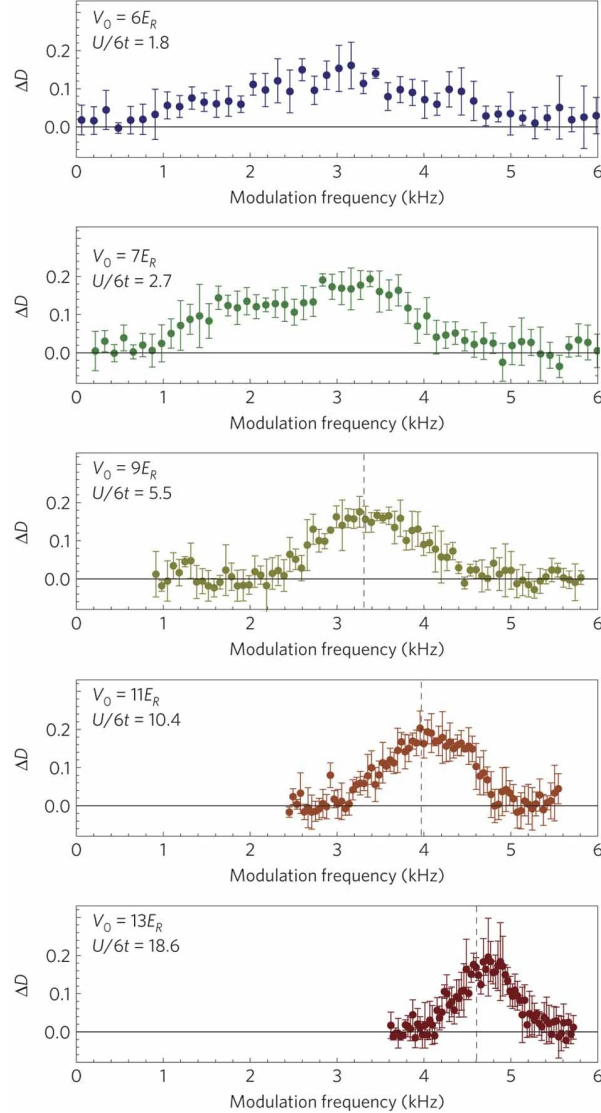


Figure 6. Lattice modulation spectra obtained for samples with $N = 1.9(1) \times 10^4$ particles and initial entropy per particle $s/k_B = 1.9(2)$, for different values of the lattice depth in E_R . The panels show the emergence of a peak centered around the frequency corresponding to the Mott gap (i.e. the measured values of on-site interaction U/t for the corresponding lattice depth). Figure reprinted with copyright permission of Ref. [74].

3.1.2. Mott Crossover in three-dimensional OLs

The Munich group has investigated the equation of state (EoS) of the SU(3) and SU(6) FHM in a cubic 3D optical lattice [78]. The relevance of this study is three-fold: First, the experimental investigation of the EoS for the density $n(\mu, T, N, U)$ for a wide range of chemical potentials and interaction strengths. Second, the experimental evidence of the metal-to-insulator crossover via the experimental determination of the local compressibility. Third, the lack of thermometry in the experiments at $U \approx W$ served as a motivation for the development of more sophisticated numerical methods to

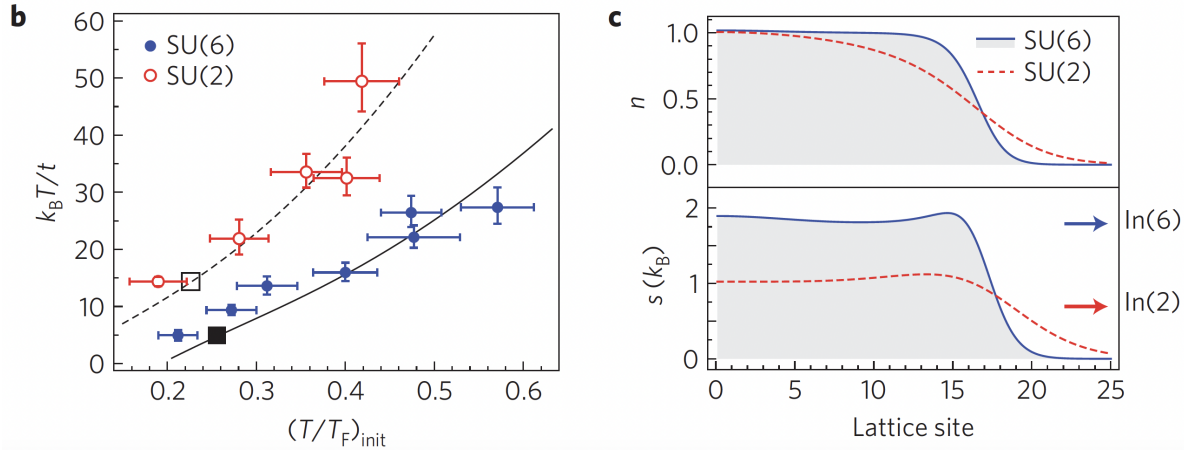


Figure 7. Results are presented for $N = 1.9(1) \times 10^4$ particles and $U/6t = 10.47$. b) Temperatures of the SU(6) (blue circles) and SU(2) (red open circles) Fermi gases after adiabatic loading in the lattice as a function of the initial temperature. c) Density and entropy profiles at the lowest temperatures indicated by squares in b) for SU(6) (blue solid line) and SU(2) (red dashed line). Figure modified with copyright permission of Ref. [74].

analyze this system.

In this experiment, the SU(N) FHM was realized by preparing a degenerate Fermi gas of ^{173}Yb with $N = 6$ equally populated spin components via evaporative cooling in a crossed dipole trap. At the end of evaporation, the Munich group had 5×10^3 atoms per spin state at temperature $T = 0.07T_F$. For the experiments with $N = 3$, they remove individual spin components by driving the $^1S_0 \rightarrow ^3P_1$ optical transition in the presence of a homogeneous magnetic field that lifts the spin-state degeneracy, and are left with an SU(3) Fermi gas at $T = 0.15T_F$ with a residual fraction of unwanted spin components below 5%. Atoms are then loaded into an optical lattice with lattice constant $d = 380$ nm. The lattice depth was varied from $3-15E_R$ to achieve $U/12t \in [0.128, 11.0]$.

Figs. 8 and 9 summarize the main results of the experiment. In Fig. 8 the authors present the experimentally measured density as a function of the chemical potential for different values of the interaction strength U/t . These results highlight that for $U \ll t$, the system is metallic and can be approximately described by the non-interacting theory for $n < 1$ (see Fig. 8a), whereas for $U \gg t$, the single site limit is a good approximation and can provide a good interpretation of the data (see Fig. 8c). However, for interactions of the order of the bandwidth $U \sim W$ (Fig. 8b), the system is a strongly correlated many-body state and at the time of publication in 2016 there were no numerical techniques to compare against.

In Fig. 9, the authors exploit the model-free access to the EoS for the density to measure the local compressibility $\tilde{\kappa} = n^2 \kappa = \partial \langle n \rangle / \partial \mu|_T$. In the strongly-interacting case

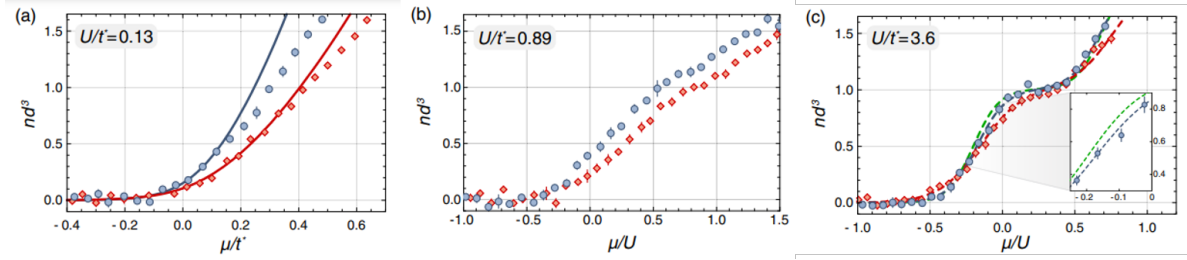


Figure 8. Density as a function of the chemical potential for $N = 3$ (red diamonds) and $N = 6$ (blue squares) Fermi gases in a 3D lattice. Here $t^* = 12t = W$ is the non-interacting bandwidth of the 3D lattice. a) $U/t^* = 0.128$ b) $U/t^* = 0.89$ c) $U/t^* = 3.6$. Solid lines are fits to the non-interacting Fermi gas EoS for densities below 0.5. Dashed lines are a second-order high temperature series expansion to extract the temperature (in green for $N = 2$ for comparison). Figure modified with copyright permission of Ref. [78].

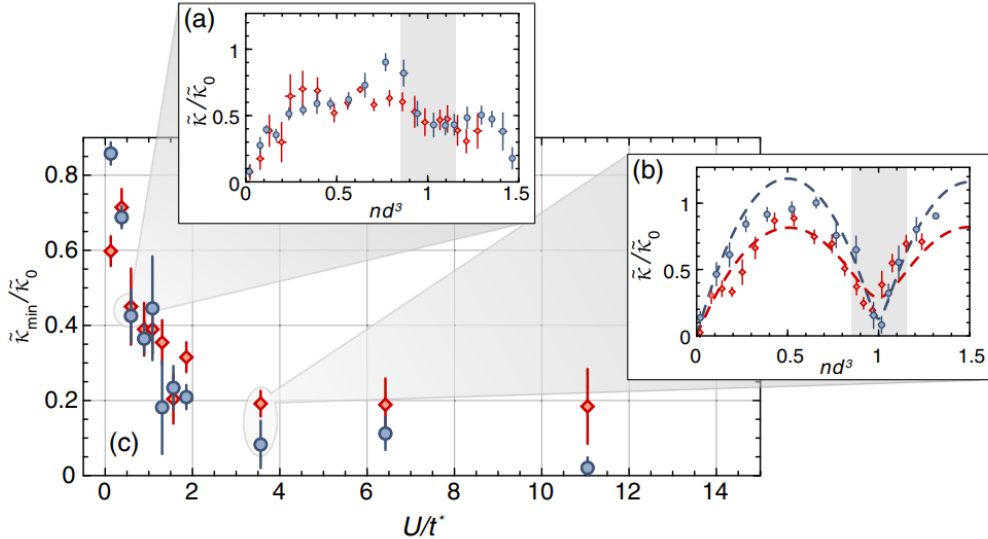


Figure 9. Compressibility for $N = 3$ (red diamonds) and $N = 6$ (blue squares) Fermi gases in a 3D lattice. Here $t^* = 12t = W$ is the non-interacting bandwidth of the 3D lattice. Insets correspond to the compressibility as a function of density at a) $U/t^* = 0.59$, and b) $U/t^* = 3.6$. Dashed lines are a second-order high temperature series expansion. c) Minimal compressibility $\tilde{\kappa}_{\min}$ as a function of the interaction strength, where $\tilde{\kappa}_0$ is the compressibility of the non-interacting SU(6) FHM at $\langle n \rangle = 1$. Figure reprinted with copyright permission of Ref. [78].

[see Fig. 9(b)], the compressibility is suppressed around $\langle n \rangle = 1$, which is consistent with the opening of charge gap and the development of a Mott insulator. In addition, the Mott crossover is studied in Fig. 9(c) where the minimum of the compressibility in the region $0.85 < \langle n \rangle < 1.15$ is presented as a function of the interaction strength. The minimum in the compressibility exhibits a suppression of roughly 1 order of magnitude and saturates at a minimum value for large U/t , indicating the system is deep in the Mott insulating state.

3.1.3. EoS and Mott Crossover in two-dimensional OLs

Building upon their previous work, the Munich group recently realized a precise characterization of the equation of state of the $SU(N)$ FHM in the two-dimensional (2D) square lattice for $N = 3, 4, 6$, and the results of their experiment are reported in Ref. [79]. The relevance of this study lies in: (1) The implementation of a 2D single-layer $SU(N)$ ensemble which can be probed with perpendicular absorption imaging with a resolution of a few lattice sites. (2) The opportunity to benchmark state-of-the-art numerical methods that were recently developed and adapted to explore the $SU(N)$ FHM in experimentally accessible regimes, such as determinant quantum Monte Carlo (DQMC) and Numerical Linked Cluster Expansions (NLCE) [63, 80, 81]. (3) The experimental demonstration of thermometry for $SU(N)$ Fermi gases in OLs in a model-independent way using the fluctuation-dissipation theorem (FDT).

In this experiment, the $SU(N)$ FHM was realized by first loading a spin-balanced mixture of approximately 1.6×10^6 ^{173}Yb atoms from a magneto-optical trap into a crossed optical dipole trap, where evaporative cooling is performed down to $T/T_F^{(3D)} < 0.2$. Subsequently, a second stage of evaporative cooling is performed in the presence of an optical gradient, yielding an ensemble of $N \sim 2 \times 10^3$ atoms in the central plane of a vertical lattice with wavelength $\lambda = 759$ nm and lattice spacing $d_{\text{vertical}} = 3.9\mu\text{m}$. In this configuration, the authors implemented a 2D single-layer $SU(N)$ ensemble with lattice spacing for $d = 380$ nm. The implementation of a single-layer is crucial, as it avoids integration over inhomogeneous stacks of 2D systems. It also allows for direct access to the density profile without the reconstruction techniques previously required in Ref. [78], and which allows for the measurement of density fluctuations. The density distribution is measured using *in situ*, saturated absorption imaging with a spatial resolution of approximately $2\mu\text{m} \approx 5d$.

The main results of this experiment are summarized in Figs. 10 and 11. In Fig. 10 the authors present the experimentally measured densities (circles) and photoassociated parity projected measurements (diamonds) as a function of the chemical potential for different values of N and the interaction strength U/t . The fit of the EoS was performed in two dimensions, with the temperature T and the chemical potential at the center of the trap μ_0 as the free parameters, where the local density approximation was used to incorporate the contributions of the trap confinement [82]. For $U/t = 7.5$ and $U/t = 10$ experiments fitted both DQMC and NLCE, observing an excellent agreement between the theory and the experiment yielding consistent fitting parameters for the two different numerical methods. For $U/t = 33$, results from NLCE and a second order HTSE also display excellent agreement. For $U/t = 2.3$ the temperature lies below the range of convergence of NLCE and experiments resorted to DQMC alone.

In addition to the total density, in Fig. 10 the authors also characterized the number of double occupancies in the model by removing doublons via photoassociation. When

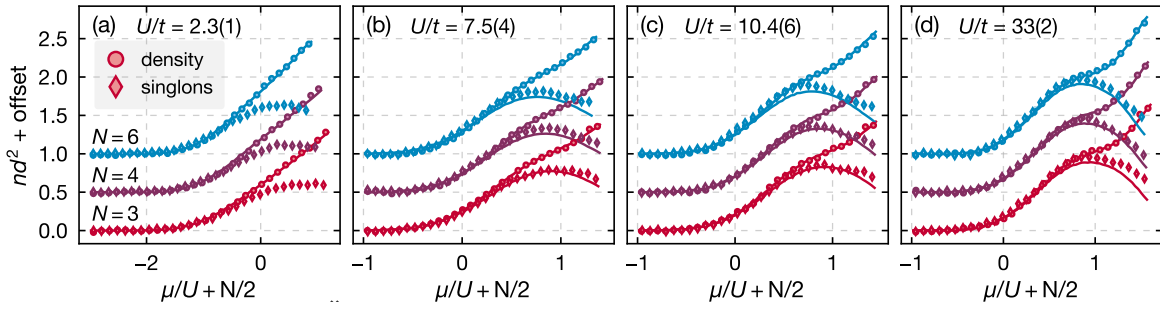


Figure 10. Equation of state for the $SU(N)$ FHM for $N = 6$ (blue), $N = 4$ (purple), and $N = 3$ (red). Density (circles) and parity projected measurements (diamonds) are presented as a function of the chemical potential for different interaction strengths (a) $U/t = 2.3$, (b) $U/t = 7.5$, (c) $U/t = 10.48$, and (d) $U/t = 33.2$. Solid lines associated to the density curves correspond to the fit of the EoS to DQMC (a) and NLCE (b)-(d) to realize thermometry. The results from the fit models are also used to calculate the parity projected measurements. All spin mixtures were prepared with the same initial entropy per particle $s/k_B = 1.2$ in the bulk before loading into the lattice. Figure modified with copyright permission of Ref. [79].

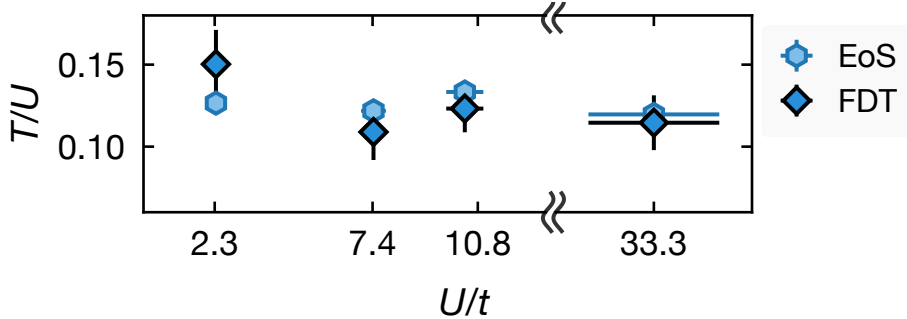


Figure 11. Comparison of the temperatures obtained using the fluctuation-dissipation theorem (FDT) [dark blue diamonds] and the fits to the equation of state (EoS) [light blue hexagons]. Error bars are the standard error of the mean. Figure modified with copyright permission of Ref. [79].

available, the NLCE prediction (lines) based on the density's fit and without any further free fit parameters was compared to the experimental observations (diamonds), and they correspond well with the experimental data. Because of the possibility to directly access the density in the 2D single-layer, measurement of density fluctuations could be performed. By measuring the density fluctuations, the FDT connects the variance of the detected atom number to the isothermal compressibility κ and the temperature T , providing model-free thermometry [83, 84]. In Fig. 11, the authors compared the temperature obtained using the FDT (squares) against the temperature returned by the fit to the EoS (hexagons), and observed good agreement for all interaction strengths.

3.1.4. Flavor-selective localization in three-dimensional OLs

In a recent experiment, the Florence group realized flavor-selective Mott localization in an $SU(3)$ Fermi gas in a 3D optical lattice [85]. This study is relevant because it

corresponds to: (1) The experimental realization of multicomponent Hubbard physics with coherent internal couplings. (2) The experimental achievement of studying Mott physics while explicitly breaking the $SU(3)$ symmetry. In this experiment, a three-component ultracold ^{173}Yb mixture with total atom number $N = 4 \times 10^4$ at an initial temperature of $T \approx 0.2T_F$ was used, which was loaded into a 3D cubic OL with lattice constant $d = 380$ nm. As previously discussed, AEAs in OLs are well described by the $SU(N)$ symmetric FHM [see eq. (9)]. In this experiment, the authors explicitly broke the $SU(N)$ symmetry by introducing the following term

$$H_R = \frac{\Omega}{2} \sum_i \left(c_{i\sigma}^\dagger c_{j\tau} + \text{h.c.} \right), \quad (10)$$

which describes a coherent on-site coupling between spin flavors σ and τ . This coupling is provided by a two-photon Raman process with Rabi frequency Ω . At the single particle level, this Raman coupling lifts the degeneracy between the spin flavors, by creating two dressed states $|\pm\rangle = (|\sigma\rangle \pm |\tau\rangle)/\sqrt{2}$, with energy shifts $\pm\Omega/2$ relative to the other spin flavors (see Fig. 12).

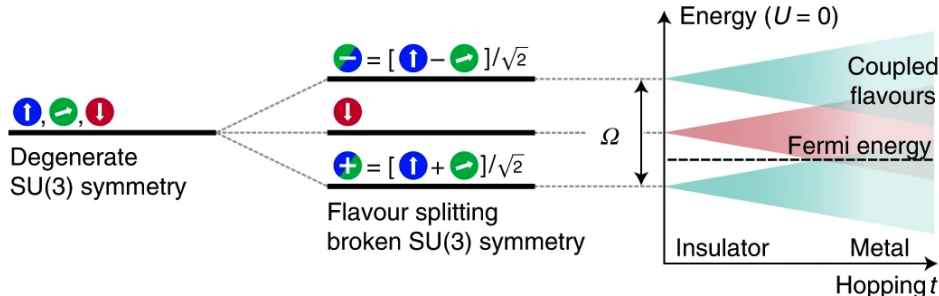


Figure 12. The Raman coupling lifts the degeneracy between the states, creating two dressed states with different energies. The competition with the hopping can drive a metal-to-insulator transition already in the non-interacting case. Figure modified with copyright permission of Ref. [85].

The coherent coupling between states $m_I = 5/2$ and $m_I = 1/2$ was realized by using a two photon σ^+/σ^- Raman transition. In this scheme, the Raman coupling is implemented with two co-propagating laser beams with wavelength $\lambda = 556$ nm and angular frequencies ω and $\omega + \delta\omega$, which are blue-detuned by 1.754 GHz with respect to the $^1S_0 \rightarrow ^3P_1$ ($F = 7/2$) recombination transition to reduce inelastic photon scattering. A 150 G magnetic field is used to define a quantization axis and to lift the degeneracy between the six hyperfine states of ^{173}Yb ground state manifold, which are split by $207 \times m_I$ Hz/G. The σ^+/σ^- coupling between $m_I = 5/2$ and $m_I = 1/2$ is obtained by setting the polarization of the two beams to be orthogonal with respect to the quantization axis and by adjusting $\delta\omega/2\pi$ to compensate the Zeeman splitting and the residual Raman light shift between the two states [73]. For measurements at $\Omega = 0$, the authors utilized optical pumping of the $^1S_0 \rightarrow ^3P_1$ transition to prepare a balanced mixture

in the hyperfine states $m_I = \pm 5/2, 1/2$. While for measurements at $\Omega \neq 0$, the loading procedure started with a 2-component unbalanced mixture of atoms in states $m_I = \pm 5/2$, such that $N_{5/2} = 2N/3$ and $N_{-5/2} = N/3$. Then after loading the lattice, the Raman beams were turned on far detuned from any two photon transitions, and an adiabatic frequency sweep was performed to bring them resonant to the $5/2 \leftrightarrow 1/2$ transition. This procedure corresponds to an adiabatic passage that brings an atom in the $m_I = 5/2$ state to the lowest energy dressed state $|+\rangle = (|5/2\rangle + |1/2\rangle)/\sqrt{2}$. At the end of the process, the population is equally distributed between the three hyperfine states.

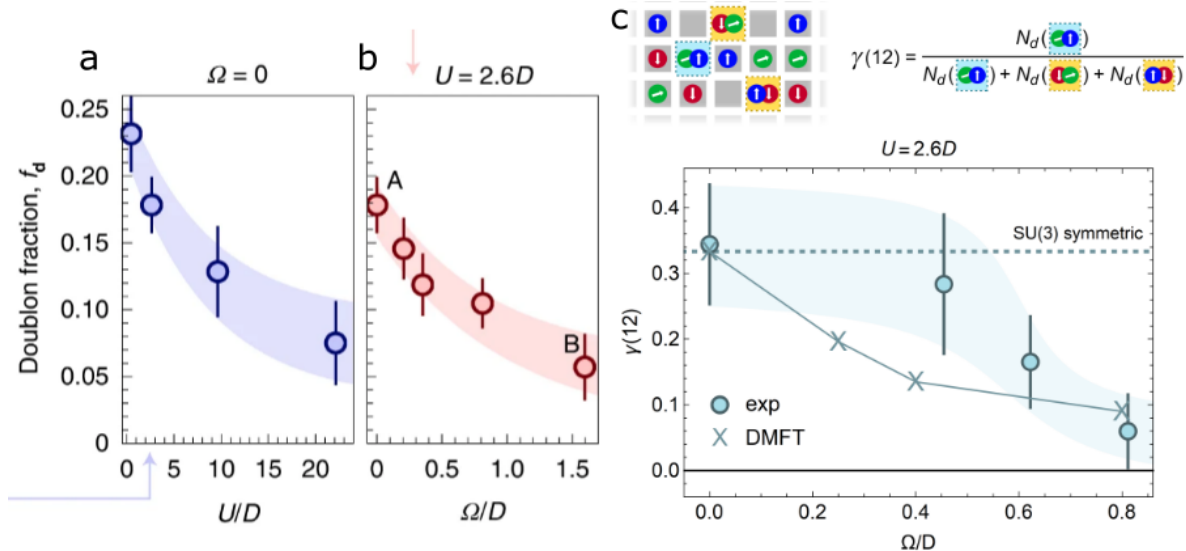


Figure 13. Average doublon fraction f_d as a function of (a) U/D at $\Omega = 0$ (b) Ω/D at $U/D = 2.6$. Here $D = 6t = W/2$ is half the bandwidth. (c) $\gamma(12)$ measures the number of atoms forming doublons in the $|5/2, 1/2\rangle$ channel, normalized by the total number of atoms forming doublons. Figure modified with copyright permission of Ref. [85].

The main results of this experiment are summarized in Fig. 13. In Figs. 13(a)-(b) the authors study the behavior of the number of double occupancies as an indicator of the degree of the Mott insulating nature of the system. While in Fig. 13(a) the emergence of an SU(3) Mott insulator is indicated by the expected suppression of the doublon fraction as the interaction strength increases, Fig. 13(b) illustrates that the doublon fraction decreases as the Rabi coupling increases, leading to a similar Mott localized state. Fig. 13(c) demonstrates that the double occupancies are flavor-dependent when $\Omega > 0$. In this figure, $\gamma(12) = N_d(12)/N_d$ is the number of atoms forming doublons in the $|5/2, 1/2\rangle$ channel normalized by the total number of atoms forming doublons. In the absence of Raman couplings ($\Omega = 0$) the results agree with the $N = 3$ symmetric expectation value (dotted line). As Ω increases, the SU(3) symmetry is broken and $\gamma(12)$ diminishes, approaching zero as $\Omega \approx D = 6t = W/2$ half the bandwidth. Doublons acquire a flavor-selective behavior, since doublon formation in the $|5/2, 1/2\rangle$ channel is suppressed because

it requires fermions in both the $|\pm\rangle$ states which have an additional energy cost of $\Omega/2$ in contrast to the other two channels $|-\frac{5}{2}, \frac{1}{2}\rangle$ and $|\frac{5}{2}, -\frac{5}{2}\rangle$.

3.2. Quantum Magnetism

In this sub-section, we review some pioneering experiments that investigated quantum magnetism in the $SU(N)$ FHM.

3.2.1. Antiferromagnetic spin correlations in a dimerized lattice

In Ref. [86], the Kyoto group reported their measurements of nearest-neighbor antiferromagnetic (AFM) correlations in a Fermi gas with $SU(4)$ symmetry in an optical superlattice. The importance of these results are two-fold. First, at a fixed entropy per particle, AFM nearest-neighbor correlations are enhanced for $N = 4$ compared with $N = 2$. Second, it was the first experimental utilization of the single-triplet oscillation technique [87] to measure nearest-neighbor spin correlation functions for $N > 2$, and set up the basis to measure those in lattices with uniform tunnelings, which were further reported in Ref. [88]. In this experiment, the $N = 2$ and the $N = 4$ FHMs were realized by loading ^{173}Yb in an optical superlattice with wavelengths $\lambda = 1064$ and $\lambda = 532$ nm, for the long and short lattice, respectively. During evaporative cooling, optical pumping is performed to create $SU(2)$ or $SU(4)$ samples. After loading into the lattice, nearest-neighbor AFM correlations between adjacent sites in the optical superlattice were measured using the singlet-triplet oscillation (STO) technique, which we describe below.

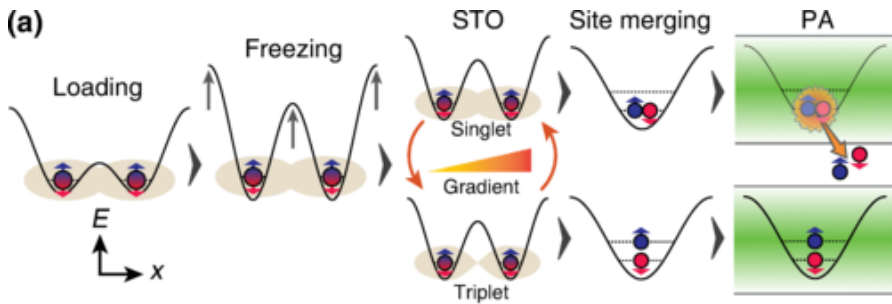


Figure 14. (a) Detection sequence for singlets and triplets in a dimer. Shown is the case of two spins per dimer. Figure modified with copyright permission of Ref. [86].

The STO technique is presented in Fig. 14. In this method, after atoms are loaded into the lattice, the lattice depth is ramped up to suppress tunneling, and freeze atoms in place. Then a spin-dependent gradient beam is used to induce oscillations between the singlet and triplet states. Depending on the STO time, the spins form a doublon in the lowest band or a state with one spin in the lowest band and the other one in the first excited band after sites are merged. Performing photoassociation, the double occupancies are removed and the associated particle loss is measured, which is proportional

to the spin-spin correlation function.

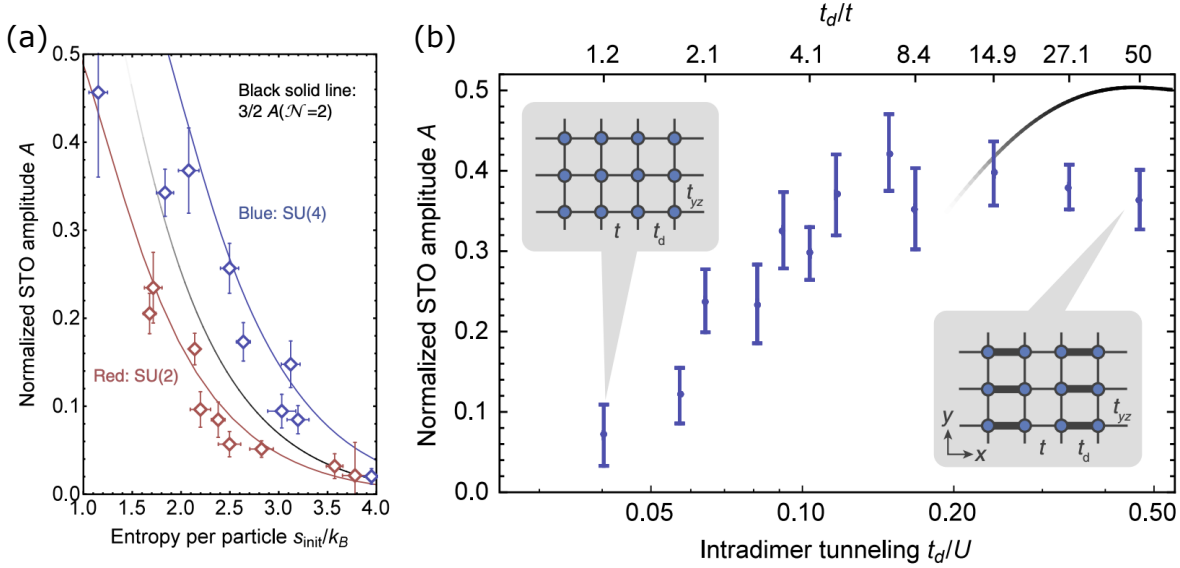


Figure 15. The normalized STO amplitude in a dimerized lattice as a function (a) the initial entropy per particle and (b) the intradimer tunneling t_d at $U/h = 3.0$ kHz. (a) Red (blue) markers correspond to $N = 2$ ($N = 4$) and results are presented for $t_d/t = 27$. (b) Results for $N = 4$. Here the tunneling rates vary from $t \in [28.0, 100]$ Hz, and $t_{yz}/t \in [1.7, 1.0]$. Figure modified with copyright permission of Ref. [86].

The main results are summarized in Fig. 15, where the authors present the normalized STO amplitude A as a function of (a) the initial entropy per particle and (b) the intradimer tunneling. In Fig. 15(a) the authors show that the normalized STO amplitude decreases as the initial entropy per particle increases since the triplet states become thermally populated. Furthermore, they demonstrate that antiferromagnetic correlations are enhanced in the $SU(4)$ system compared to $SU(2)$ for the same initial entropy. This enhancement is due to the difference of the fraction of singlet configurations among all possible states $\binom{N}{2}$, and the cooling effect related to spin entropy that was previously observed [74]. In Fig. 15(b) the authors discuss the dependence of A on the intradimer tunneling rate t_d . As t_d decreases, the normalized STO amplitude decreases because the excitation energy to the triplet state is lowered, which in the two particle two site sector, is given by $-U/2 + \sqrt{16t_d^2 + U^2}/2$. The experimental data suggests that although nearest-neighbor antiferromagnetic correlations get smaller as t_d is lowered, they should retain a non-vanishing amplitude in the isotropic lattice.

3.2.2. Antiferromagnetic spin correlations in OLs with uniform tunnelings

Building upon their previous work in strongly dimerized optical lattices, the Kyoto group then measured $SU(N)$ antiferromagnetic nearest-neighbor spin correlations in OLs with isotropic tunnelings. Besides being the first experimental determination of

$SU(N)$ AFM correlations in lattices with homogeneous tunnelings, an important milestone of this study corresponds to the creation of the coldest fermions ever created in nature in absolute temperature and in cold atoms. In this experiment, spin-balanced mixtures of 2.4×10^4 ^{173}Yb atoms are adiabatically loaded into 1D, 2D and 3D cubic OLs with lattice constant $d = 266$ nm. To achieve the lower dimensional lattices, a strong tunneling anisotropy is introduced in one or two directions to suppress tunneling in that direction (the inter-lattice tunneling is $\lesssim 5\%$ than the intra-lattice tunneling).

After loading into the lattice, nearest-neighbor AFM correlations were measured using the STO technique. Similarly to Ref. [86], the application of a spin-dependent potential gradient before the merging process drives oscillations between the singlet and the triplet states in two adjacent sites. Such spin-dependent potential gradient is generated by applying an optical Stern–Gerlach laser beam close to the $^1S_0 \rightarrow ^3P_1$ resonance, with a detuning of +2.6 GHz from the $F = 5/2 \rightarrow 7/2$ transition, which minimizes the ratio of the photon scattering rate to the differential light shifts. Experiments measure the fraction of both singlet and triplet states formed within nearest-neighbour lattice sites. It is important to notice that the naming “singlet” and “triplet” in this context corresponds to the $SU(N)$ counterparts of the $SU(2)$ double-well singlets and triplets, and should not be confused with $SU(N)$ singlets and triplets, which are N -body entangled states [70].

The detected $SU(N)$ counterpart of the $SU(2)$ double-well singlet is a $\binom{N}{2}$ -fold multiplet of the form $(|\sigma, \tau\rangle - |\tau, \sigma\rangle)/\sqrt{2}$, while the the double-well triplet is a $[(\binom{N}{2}) + N]$ -fold multiplet, among which the $\binom{N}{2}$ states of the form $(|\sigma, \tau\rangle + |\tau, \sigma\rangle)/\sqrt{2}$ are detected by the STO scheme, while the case $\sigma = \tau$ is not. The STO measurement is valid only if the contribution from multiple occupancies can be neglected, and therefore the authors set the density at the center of the trap to one particle per site on average, and set the interaction strength to a large value of $U/t = 15.3$ to strongly supress the formation of double and higher occupancies.

The main results of the manuscript are summarized in Figs. 16 and 17. In Fig. 16 the authors present the experimentally measured STO imbalance I and amplitude A for $SU(6)$ and $SU(2)$ Fermi gases in 1D and 3D OLs as a function of entropy per particle. The imbalance and the amplitude are defined as,

$$A = -\frac{1}{N_{\text{ptcl}}} [C_{\text{NN}}]_{\text{total}} \quad (11)$$

$$I = \frac{2A}{A + [n(i)n(i+1)]_{\text{total}}/N_{\text{ptcl}}}, \quad (12)$$

where $\langle n(i)n(i+1) \rangle$ is the nearest-neighbor density–density correlation function, and

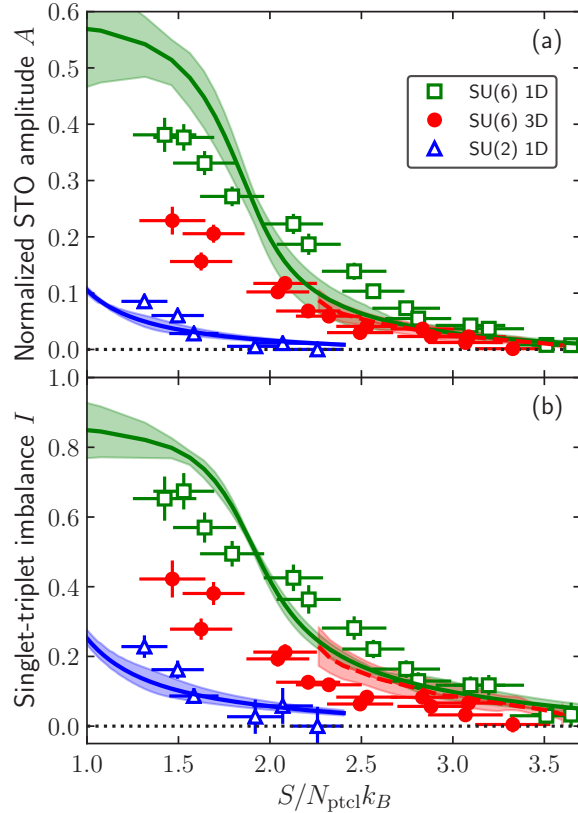


Figure 16. Entropy dependence of the (a) normalized STO amplitude A (b) singlet-triplet imbalance I . Results are presented for 1D and 3D lattices, showing experimental data for the SU(6) 1D (green squares), SU(6) 3D (red circles) and SU(2) 1D systems (blue triangles). Horizontal error bars represent the standard deviation of ten entropy measurements, while vertical error bars are extracted from the fitting errors in the analysis of the STO signal. Numerical calculations with ED (solid lines) and DQMC (dashed lines) are also displayed. Shaded areas represent uncertainty from the systematic and statistical errors of the numerical methods plus the possible systematic error (20%) in the total atom number measurement. Figure modified with copyright permission of Ref. [88].

C_{NN} is the nearest-neighbor spin-spin correlation function,

$$C_{\text{NN}} = \sum_{\sigma \neq \tau} \left[\langle n_{\sigma}(i) n_{\sigma}(i+1) \rangle - \langle n_{\sigma}(i) n_{\tau}(i+1) \rangle \right], \quad (13)$$

which measures the likelihood of having a different spin flavors on adjacent sites. In the local-density approximation (LDA),

$$[\mathcal{O}]_{\text{total}} = \int \frac{d^3 r}{d^3} \langle \mathcal{O}(\mu(\mathbf{r}, T)) \rangle \quad (14)$$

for an arbitrary observable \mathcal{O} .

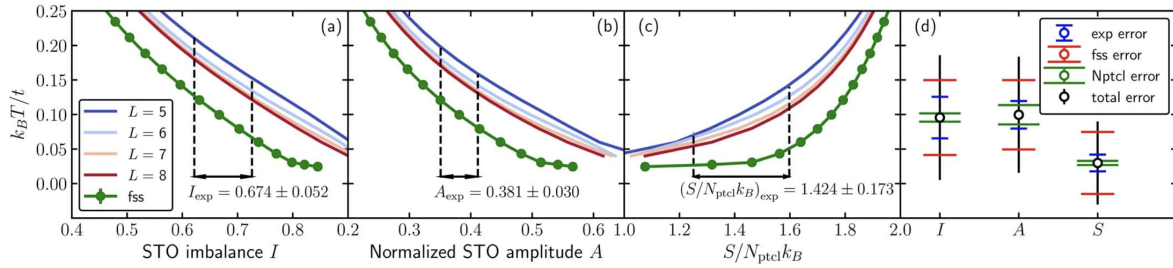


Figure 17. Thermometry of an SU(6) Fermi gas in a one-dimensional OL at $U/t = 15.3$. (a)-(c) Solid lines correspond to exact diagonalization results in L sites chains. Green circles and lines correspond to finite-size extrapolations. Dashed vertical lines correspond to the range of the largest experimentally measured STO imbalance in 1D that is consistent with error bars. (d) Extracted temperatures from the STO imbalance, amplitude and the initial entropy per particle. Error bars come from the measured correlations error bars (blue), the finite-size error (red), the particle number fluctuation (green), and their sum (black). Figure reprinted with copyright permission of Ref. [88].

Fig. 16 demonstrates that at fixed entropy per particle, AFM nearest-neighbor spin correlations get enhanced as N increases, and also that these correlations appear at higher entropy for larger N . This last point can be easily interpreted deep in the Mott regime at $1/N$ filling, in which the minimum entropy per site attainable before any correlations develop is $\ln(N)$. As the temperature is lowered, entropy is lowered as correlations develop. Furthermore, it illustrates the dimensionality dependence, with the 1D case exhibiting the largest correlations. This behaviour is similar to previous studies in an SU(2) system [87, 89, 90] and can be understood at sufficiently high temperatures. In this regime, correlations depend only on temperature not dimension, and decrease with increasing temperature. Additionally, as the dimensionality decreases, the bandwidth also decreases, and therefore, at fixed entropy, the temperature decreases. These arguments together imply that correlations decrease as the dimensionality is increased. The authors observed that the experimental data show reasonable agreement with theoretical predictions obtained by exact diagonalization (ED) for 1D and by determinant quantum Monte Carlo (DQMC) for 3D, without any fitting parameters. In the case of $N = 6$ in 3D, the experiments reach entropies below the regime where the calculations converge, highlighting the importance of these experiments as quantum simulations, and providing motivation for the development and refinement of numerical techniques to mitigate the sign problem to reach lower temperatures [91, 92].

At that time, this experiment did not have the capabilities to directly measure the temperature at the very low entropies studied. However, for the 1D systems, the temperature was inferred by comparing experiment and theory. In 1D, the lowest temperature achieved in the experiments corresponds to $k_B T / t = 0.096 \pm 0.054 \pm 0.030$, obtained from the experimentally measured STO imbalance I at $S/N_{ptcl} k_B = 1.45 \pm 0.05$. The first error bar corresponds to the finite-size error of the calculations, and the second

one corresponds to the experimental errors in the correlation measurements. The details of the thermometry are presented in Fig. 17, where estimates of the temperature using A instead of I , yield consistent results. For comparison, to obtain the same singlet–triplet imbalance, the $N = 2$ system should be at $S/N_{\text{ptcl}}k_B = 0.499 \pm 0.136 \pm 0.120$. Since the state-of-the-art experiments of the SU(2) FHM with alkali atoms in OLs perform at an entropy per particle $\sim 1k_B$ [93], this suggests an experimental advantage for SU(N) systems in obtaining highly correlated states in optical lattices.

3.3. Overview of computational and theoretical works on SU(N) lattice models

Historically, the study of SU(N) quantum magnetism arose from the mathematical technique of large- N expansions [65–69]. However, the possibility of exploiting the inherent SU(N) symmetry of AEAs what has attracted more attention to SU(N)-symmetric Hamiltonians, both theoretically and experimentally [26, 60, 61, 147]. In the last decade, a series of theoretical predictions and state-of-the art numerical calculations have been performed on the SU(N) FHM for different values of N at $T = 0$, finite temperature, filling fractions, and for various geometries and limits. In all of these cases, the SU(N) lattice models are predicted to display a variety of interesting phases with novel and rich properties depending on the value of N . For instance even at weak-to-intermediate coupling, the SU(N) FHM can host phases other than the SU(N)-Fermi liquid that we have discussed in this paper. An interesting example of this is the staggered flux phase, where the lattice translation symmetry is spontaneously broken; this phase naturally arises in the large N limit.

Furthermore, the strong-coupling limit of the FHM is also of great interest. In particular, at $1/N$ -filling (where $U \gg t$ and there is one particle per site on average). In this case, the system is described by the SU(N) Heisenberg model:

$$H = \frac{2t^2}{U} \sum_{\langle i,j \rangle} S_\alpha^\beta(i) S_\beta^\alpha(j), \quad (15)$$

where the spin operators, $S_\alpha^\beta = c_\alpha^\dagger c_\beta$ now obey the SU(N) algebra. This model can host a zoo of exotic phases in two dimensions. For instance, at large N , it can host the non-magnetic lattice-symmetry breaking valence cluster state, and the chiral spin liquid which supports topological fractional excitations [138]. Interestingly, this model can support ordered states at smaller N for other lattice geometries. For instance, the SU(3) Heisenberg model hosts a three-sublattice state in a triangular lattice [133, 134] and a dimerized magnetically ordered state on a honeycomb lattice [148–150]. Finally, we note that in a recent study, Yamamoto *et al.* have demonstrated the existence of nematic phases in the SU(3) Heisenberg model on a triangular lattice in the presence of low and high magnetic fields [143].

In this review, we chose to focus on the experimental achievements of quantum simulators with AEAs in optical lattice. However, there is an abundant amount of

Table 1. Short compendium of the theory of $SU(N)$ Lattice models.

| Model | N | Geometry | T | Methods | References |
|------------|----------|-------------------------------|------|----------------------------|------------|
| Hubbard | 2-4, 6 | Square | F | DQMC, NLCE, HTSE, ED | [80] |
| Hubbard | 3 | Square | F | DQMC, NLCE | [81] |
| Hubbard | 3 | Square | 0 | CPQMC | [91] |
| Hubbard | ≥ 2 | Square | F | RG, MF | [94] |
| Hubbard | 2,4,6 | Square | 0 | Projector QMC | [95] |
| Hubbard | 6 | Square | 0 | Projector QMC | [96] |
| Hubbard | 2,4,6 | Square | F | DQMC | [97] |
| Hubbard | 2-4 | Square | F | HTSE | [98] |
| Hubbard | 4 | Square | 0 | Projector QMC | [99, 100] |
| Hubbard | 4 | Square | F | DMFT | [101] |
| Hubbard | 3-10 | Square | 0 | SRMF | [102] |
| Hubbard | 4 | Square | F | DMFT | [103] |
| Hubbard | 6 | Square | F | FLT | [104] |
| Hubbard | 2-6 | Square | 0 | ED | [105] |
| Hubbard | 6 | Square | F | Diagrammatic QMC | [106] |
| Hubbard | 2,4,6,8 | Square | 0 | large- N , Projector QMC | [107] |
| Hubbard | 2,4,6 | Square, Honeycomb | 0 | Projector QMC | [108] |
| Hubbard | 2-6 | Square, Honeycomb, Triangular | 0 | ED | [109] |
| Hubbard | 3 | Square, Cubic, Bethe | F | DMFT, VMC | [110] |
| Hubbard | 3 | Square, Cubic | F | DMFT | [111] |
| Hubbard | 3 | Cubic | F | DMFT | [112] |
| Hubbard | 2-5 | Chain | 0 | DMRG, BA, Bos | [113] |
| Hubbard | 2-4,6,10 | Chain | F | SSE-QMC | [114] |
| Hubbard | 2,3,4 | Chain | 0 | GFMC | [115] |
| Hubbard | 4-14 | Chain | F | SSE-QMC | [116] |
| Hubbard | 3 | Chain | 0 | DMRG | [117] |
| Hubbard | 2-5 | Chain | 0 | DMRG | [118] |
| Hubbard | 4 | Chain | 0 | BA, DMRG | [119] |
| Hubbard | 2-6 | Chain | F | DMRG | [120] |
| Hubbard | 4 | Honeycomb | F | HTSE | [121] |
| Hubbard | 4,6 | Honeycomb | 0 | Projector QMC | [122] |
| Hubbard | 4,6 | Honeycomb | F | DQMC | [123] |
| Hubbard | 3 | Honeycomb | 0 | Projector QMC | [124] |
| Hubbard | ≥ 2 | Bipartite 2D | F | HTSE | [125] |
| Hubbard | 3 | Triangular | F | DMFT | [126–128] |
| Hubbard | 2,3 | Lieb | 0,F | MF | [129] |
| Hubbard | 2,4,6 | | F | HTSE | [130] |
| Hubbard | 2-5 | | F | DMFT | [131] |
| Hubbard | 2-6 | | F | DMFT | [132] |
| Heisenberg | 3 | Square, Cubic | 0 | ED | [133] |
| Heisenberg | 3 | Square, Triangular | 0 | DMRG, iPEPS | [134] |
| Heisenberg | 4 | Square | 0 | ED, iPEPS | [135] |
| Heisenberg | ≥ 2 | Square | 0 | large- N | [136] |
| Heisenberg | 5,8,10 | Square | 0 | ED | [137] |
| Heisenberg | ≥ 2 | Square | 0 | large- N | [138] |
| Heisenberg | 2-5 | Chain | F | CTWLMC | [139] |
| Heisenberg | 3,4 | Chain, Square, Triangular | F | HTSE, ED | [140] |
| Heisenberg | > 2 | Chain | 0 | CFT, ED, DMRG | [141] |
| Heisenberg | 4 | Honeycomb | 0 | MF, VMC | [142] |
| Heisenberg | 3 | Triangular | 0, F | CMF, semiclassical MC | [143] |
| Heisenberg | 2-9 | Triangular | 0 | MF | [144] |
| $t - J$ | 3 | Square | 0 | DMRG | [145] |
| $t - J$ | 4 | Chain | 0 | DMRG | [146] |

Abbreviations F : finite-temperature, MF: mean-field, MC: Monte Carlo, QMC: Quantum Monte Carlo, BA: Bethe-Ansatz, Bos: Bosonization, CFT: conformal field theory, CMF: cluster MF, CTWLMC: continuous-time world-line MC, CPQMC: constrained path QMC, DMFT: dynamical mean-field theory, DMRG: density matrix renormalization group, DQMC: determinant QMC, ED: exact diagonalization, FLT: Fermi liquid theory, GFMC: Green's function MC, HTSE: high-temperature series expansions, iPEPS: infinite projected entangled-pair states, NLCE: numerical linked cluster expansion, RG: renormalization group, VMC: variational MC, SRMF: slave rotor mean-field, SSE-QMC: quantum MC simulations within the stochastic series expansion (SSE).

theoretical work on $SU(N)$ models and we have highlighted only a few important works in this section. We thus believe that it would be instructive to provide a short compendium of theoretical and computational work that has been done for the $SU(N)$ lattice models. This is done in Table 3.3 where references on computational and theoretical work are presented. These works illustrate the richness of the models and motivate further experimental studies.

4. Future directions

With the development and implementation of quantum gas microscopy for AEAs [151–153], number-resolved imaging without parity projection [154], and cooling proposals specific to $SU(N)$ gases [155, 156], experiments now poise themselves to measure long range correlations and explore the plethora of proposed magnetic states (see Refs. in Table 3.3). Furthermore, a key objective in many-body physics is to understand the effects of doping Mott insulators and magnetically ordered phases. This has been an active area in the past few years for $SU(2)$ ultracold FHMs. One example of progress is the development and testing of geometric string theory [157, 158], which establishes a connection between the strongly correlated quantum states at finite doping and the AFM parent state at half-filling. Even at the current temperatures, experiments are equipped to explore the doped $SU(N)$ FHM and study the string length and anisotropy across different magnetic crossovers at finite temperature.

Exploring the spin-imbalanced $SU(N)$ FHM and the $SU(N)$ FHM under symmetry-breaking fields is an immediate question of interest to the field. These questions can be addressed in a straightforward manner by creating spin-polarized samples via optical pumping. Other possible directions of study correspond to the experimental exploration of Nagaoka ferromagnetism [105, 125], the ionic Hubbard model [159], and the $SU(N)$ FHM with Raman couplings, which is predicted to support chiral currents [160]. In addition to $SU(N)$ quantum magnetism, other interesting directions which could be readily implemented with AEAs in OLs, correspond to the study of transport properties, (such as was done for $SU(2)$ in Refs. [161, 162]), engineering hadronic matter [163], realizing collective spin models [164], and the quantum simulation of lattice gauge theories [165]. As previously mentioned, the interest in using AEAs in OLs is not limited to studying the $SU(N)$ FHM model, but also two-band models [26, 60, 166] such as the $SU(N)$ Kondo Lattice Model (KLM) [56, 57, 167, 168]. These two-band models can be implemented by using the 1S_0 ground state and the 3P_0 metastable state of AEAs, which exhibit $SU(N)$ symmetric interactions.

Finally, these systems can be a versatile arena to study far-from-equilibrium physics. There have already been a few theoretical efforts to study the effects of quantum quenches in these systems [25, 169–172]. These systems can be potentially employed to study generalized thermalization [173], and hydrodynamics [174] dynamical quantum

phase transitions [175], and the physics of non-thermal fixed points [176]. In this context, it is worth noting that although interactions between fermionic AEAs are inherently repulsive ($U > 0$), and are not tunable via magnetic Feshbach resonances as in the case of alkali atoms, the possibility to study attractive ($U < 0$) $SU(N)$ FHMs with N as large as 36 using ultracold molecules has been recently proposed [177]. This opens up the possibility of performing interaction quenches in these systems. It would also be interesting to implement periodic driving in these systems [178], thereby paving the path towards realizing Floquet phases of matter with $SU(N)$ -symmetric interactions.

Acknowledgements

EIGP is supported by the grant DE-SC-0022311, funded by the U.S. Department of Energy, Office of Science. SC thanks DST, India for support through SERB project SRG/2023/002730. We thank Kaden Hazzard for several discussions.

References

- [1] Maciej Lewenstein, Anna Sanpera, and Veronica Ahufinger. *Ultracold Atoms in Optical Lattices: Simulating quantum many-body systems*. OUP Oxford, 2012. [2](#)
- [2] Patrick Windpassinger and Klaus Sengstock. Engineering novel optical lattices. *Rep. Prog. Phys.*, 76(8):086401, 2013. [2](#)
- [3] Jae-yoon Choi. Quantum simulations with ultracold atoms in optical lattices: past, present and future. *Journal of the Korean Physical Society*, 82(9):875–881, 2023. [2](#)
- [4] Nathan Goldman, Jan C Budich, and Peter Zoller. Topological quantum matter with ultracold gases in optical lattices. *Nat. Phys.*, 12(7):639–645, 2016. [2](#)
- [5] Patrick Windpassinger and Klaus Sengstock. Specific optical lattices. In *Quantum Gas Experiments: Exploring Many-Body States*, pages 87–100. World Scientific, 2015. [2](#)
- [6] Javier Argüello-Luengo, Utso Bhattacharya, Alessio Celi, Ravindra W Chhajlany, Tobias Grass, Marcin Płodzień, Debraj Rakshit, Tymoteusz Salamon, Paolo Stornati, Leticia Tarruell, et al. Synthetic dimensions for topological and quantum phases. *Communications Physics*, 7(1):143, 2024. [2](#)
- [7] Alexander Impertro, Simon Karch, Julian F Wienand, SeungJung Huh, Christian Schweizer, Immanuel Bloch, and Monika Aidelsburger. Local readout and control of current and kinetic energy operators in optical lattices. *Phys. Rev. Lett.*, 133(6):063401, 2024. [2](#)
- [8] Yang Wang, Aishwarya Kumar, Tsung-Yao Wu, and David S Weiss. Single-qubit gates based on targeted phase shifts in a 3d neutral atom array. *Science*, 352(6293):1562–1565, 2016. [2](#)
- [9] Aishwarya Kumar, Tsung-Yao Wu, Felipe Giraldo, and David S Weiss. Sorting ultracold atoms in a three-dimensional optical lattice in a realization of maxwell’s demon. *Nature*, 561(7721):83–87, 2018. [2](#)
- [10] Aaron W Young, William J Eckner, Nathan Schine, Andrew M Childs, and Adam M Kaufman. Tweezer-programmable 2d quantum walks in a Hubbard-regime lattice. *Science*, 377(6608):885–889, 2022. [2](#)
- [11] Immanuel Bloch. Ultracold quantum gases in optical lattices. *Nature physics*, 1(1):23–30, 2005. [2](#)
- [12] Immanuel Bloch, Jean Dalibard, and Wilhelm Zwerger. Many-body physics with ultracold gases. *Reviews of modern physics*, 80(3):885–964, 2008. [2](#)
- [13] Servaas Kokkelmans. Feshbach resonances in ultracold gases. In *Quantum Gas Experiments: Exploring Many-Body States*, pages 63–85. World Scientific, 2015. [2](#)

[14] Y. Takasu, K. Komori, K. Honda, M. Kumakura, T. Yabuzaki, and Y. Takahashi. Photoassociation spectroscopy of laser-cooled Ytterbium atoms. *Phys. Rev. Lett.*, 93:123202, Sep 2004. [3](#)

[15] Kanhaiya Pandey, Alok K. Singh, P. V. Kiran Kumar, M. V. Suryanarayana, and Vasant Natarajan. Isotope shifts and hyperfine structure in the 555.8-nm $^1S_0 \rightarrow ^3P_1$ line of Yb. *Phys. Rev. A*, 80:022518, Aug 2009. [3](#)

[16] Sergey G. Porsev and Andrei Derevianko. Hyperfine quenching of the metastable $^3p_{0,2}$ states in divalent atoms. *Phys. Rev. A*, 69:042506, Apr 2004. [3](#)

[17] Jun Woo Cho, Han-gyeol Lee, Sangkyung Lee, Jaewook Ahn, Won-Kyu Lee, Dai-Hyuk Yu, Sun Kyung Lee, and Chang Yong Park. Optical repumping of triplet- p states enhances magneto-optical trapping of Ytterbium atoms. *Phys. Rev. A*, 85:035401, Mar 2012. [3](#)

[18] K. Beloy, J. A. Sherman, N. D. Lemke, N. Hinkley, C. W. Oates, and A. D. Ludlow. Determination of the $5d6s$ 3D_1 state lifetime and blackbody-radiation clock shift in Yb. *Phys. Rev. A*, 86:051404, Nov 2012. [3](#)

[19] Marianna S. Safronova, Sergey G. Porsev, Christian Sanner, and Jun Ye. Two clock transitions in neutral Yb for the highest sensitivity to variations of the fine-structure constant. *Phys. Rev. Lett.*, 120:173001, Apr 2018. [3](#)

[20] V. A. Dzuba, V. V. Flambaum, and S. Schiller. Testing physics beyond the standard model through additional clock transitions in neutral Ytterbium. *Phys. Rev. A*, 98:022501, Aug 2018. [3](#)

[21] Giulio Pasqualetti. *Probing the thermodynamics of $SU(N)$ -symmetric Fermi gases with ultracold atoms*. PhD thesis, Ludwig-Maximilians-Universität München, 2023. [3](#)

[22] C J Pethick and H Smith. *Bose-Einstein Condensation in Dilute Gases*. Cambridge University Press, 2nd edition, 2008. [3](#)

[23] Francesco Scazza. *Probing $SU(N)$ -symmetric orbital interactions with ytterbium Fermi gases in optical lattices*. PhD thesis, Ludwig-Maximilians-Universität München, 2015. [3](#)

[24] F. Scazza, C. Hofrichter, M. Höfer, P. C. De Groot, I. Bloch, and S. Fölling. Observation of two-orbital spin-exchange interactions with ultracold $su(n)$ -symmetric fermions. *Nat Phys*, 10:779, August 2014. [3](#)

[25] Chen-How Huang, Yosuke Takasu, Yoshiro Takahashi, and Miguel A. Cazalilla. Suppression and control of prethermalization in multicomponent Fermi gases following a quantum quench. *Phys. Rev. A*, 101:053620, May 2020. [3, 28](#)

[26] A. V. Gorshkov, M. Hermele, V. Gurarie, C. Xu, P. S. Julienne, J. Ye, P. Zoller, E. Demler, M. D. Lukin, and A. M. Rey. Two-orbital $SU(N)$ magnetism with ultracold alkaline-earth atoms. *Nat. Phys.*, 6:289–295, 2010. [4, 5, 10, 26, 28](#)

[27] S.-K. Yip and Tin-Lun Ho. Zero sound modes of dilute Fermi gases with arbitrary spin. *Phys. Rev. A*, 59:4653–4656, Jun 1999. [4](#)

[28] S-K Yip, Bor-Luen Huang, and Jung-Shen Kao. Theory of $SU(N)$ Fermi liquids. *Phys. Rev. A*, 89(4):043610, 2014. [6](#)

[29] Chi-Ho Cheng and S-K Yip. $SU(N)$ Fermi liquid at finite temperature. *Phys. Rev. A*, 95(3):033619, 2017. [6](#)

[30] Sylvain Capponi, Philippe Lecheminant, and Keisuke Totsuka. Phases of one-dimensional $SU(N)$ cold atomic Fermi gases—from molecular luttinger liquids to topological phases. *Annals of Physics*, 367:50–95, 2016. [6](#)

[31] Jordi Pera, Joaquim Casulleras, and Jordi Boronat. Itinerant ferromagnetism in dilute $SU(N)$ Fermi gases. *SciPost Physics*, 14(3):038, 2023. [6](#)

[32] Chen-How Huang and Miguel A Cazalilla. Itinerant ferromagnetism in $SU(N)$ -symmetric Fermi gases at finite temperature: first order phase transitions and time-reversal symmetry. *New Journal of Physics*, 25(6):063005, 2023. [6](#)

[33] Jordi Pera, Joaquim Casulleras, and Jordi Boronat. Beyond universality in repulsive $SU(N)$ Fermi gases. *SciPost Physics*, 17(2):030, 2024. [6](#)

[34] Lindsay Sonderhouse, Christian Sanner, Ross B Hutson, Akihisa Goban, Thomas Bilitewski, Lingfeng Yan, William R Milner, Ana M Rey, and Jun Ye. Thermodynamics of a deeply degenerate $SU(N)$ -symmetric Fermi gas. *Nat. Phys.*, 16(12):1216–1221, 2020. [6](#) [7](#)

[35] Guido Pagano, Marco Mancini, Giacomo Cappellini, Pietro Lombardi, Florian Schäfer, Hui Hu, Xia-Ji Liu, Jacopo Catani, Carlo Sias, Massimo Inguscio, and Leonardo Fallani. A one-dimensional liquid of fermions with tunable spin. *Nature Physics*, 10(3):198–201, 2014. [8](#)

[36] Chengdong He, Zejian Ren, Bo Song, Entong Zhao, Jeongwon Lee, Yi-Cai Zhang, Shizhong Zhang, and Gyu-Boong Jo. Collective excitations in two-dimensional $SU(N)$ Fermi gases with tunable spin. *Phys. Rev. Res.*, 2(1):012028, 2020. [8](#) [9](#)

[37] Sayan Choudhury, Kazi R Islam, Yanhua Hou, Jim A Aman, Thomas C Killian, and Kaden RA Hazzard. Collective modes of ultracold fermionic alkaline-earth-metal gases with $SU(N)$ symmetry. *Phys. Rev. A*, 101(5):053612, 2020. [8](#)

[38] Bo Song, Yangqian Yan, Chengdong He, Zejian Ren, Qi Zhou, and Gyu-Boong Jo. Evidence for bosonization in a three-dimensional gas of $SU(N)$ fermions. *Phys. Rev. X*, 10(4):041053, 2020. [8](#) [9](#)

[39] Shina Tan. Energetics of a strongly correlated Fermi gas. *Annals of Physics*, 323(12):2952–2970, 2008. [8](#)

[40] Shina Tan. Generalized virial theorem and pressure relation for a strongly correlated Fermi gas. *Annals of Physics*, 323(12):2987–2990, 2008. [8](#)

[41] Shina Tan. Large momentum part of a strongly correlated Fermi gas. *Annals of Physics*, 323(12):2971–2986, 2008. [8](#)

[42] Immanuel Bloch, Jean Dalibard, and Sylvain Nascimbène. Quantum simulations with ultracold quantum gases. *Nat. Phys.*, 8(4):267–276, apr 2012. [8](#) [10](#)

[43] Christian Gross and Immanuel Bloch. Quantum simulations with ultracold atoms in optical lattices. *Science*, 357(6355):995–1001, 2017. [8](#) [10](#)

[44] Florian Schäfer, Tkeshi Fukuhara, Seiji Sugawa, Yosuke Takasu, and Yoshiro Takahashi. Tools for quantum simulation with ultracold atoms in optical lattices. *Nat. Rev. Phys.*, 2:411–425, 2020. [8](#) [10](#)

[45] Ehud Altman, Kenneth R. Brown, Giuseppe Carleo, Lincoln D. Carr, Eugene Demler, Cheng Chin, Brian DeMarco, Sophia E. Economou, Mark A. Eriksson, Kai-Mei C. Fu, Markus Greiner, Kaden R.A. Hazzard, Randall G. Hulet, Alicia J. Kollár, Benjamin L. Lev, Mikhail D. Lukin, Ruichao Ma, Xiao Mi, Shashank Misra, Christopher Monroe, Kater Murch, Zaira Nazario, Kang-Kuen Ni, Andrew C. Potter, Pedram Roushan, Mark Saffman, Monika Schleier-Smith, Irfan Siddiqi, Raymond Simmonds, Meenakshi Singh, I.B. Spielman, Kristan Temme, David S. Weiss, Jelena Vučković, Vladan Vuletić, Jun Ye, and Martin Zwierlein. Quantum simulators: Architectures and opportunities. *PRX Quantum*, 2:017003, Feb 2021. [8](#)

[46] J. Hubbard. Electron correlations in narrow energy bands. *Proc. R. Soc. Lond. A*, 276:238–257, 1963. [8](#)

[47] Arianna Montorsi, editor. *The Hubbard Model: A reprint volume*. World Scientific Publishing Co. Pte. Ltd., 1992. [8](#)

[48] Hal Tasaki. The Hubbard model - an introduction and selected rigorous results. *J. Phys.: Condens. Matter*, 10:4353, 1998. [8](#)

[49] Daniel P. Arovas, Erez Berg, Steven A. Kivelson, and Srinivas Raghu. The Hubbard model. *Annual Review of Condensed Matter Physics*, 13(1):239–274, 2022. [8](#)

[50] Masatoshi Imada, Atsushi Fujimori, and Yoshinori Tokura. Metal-insulator transitions. *Rev. Mod. Phys.*, 70:1039–1263, Oct 1998. [9](#)

[51] S. R. White, D. J. Scalapino, R. L. Sugar, E. Y. Loh, J. E. Gubernatis, and R. T. Scalettar. Numerical study of the two-dimensional Hubbard model. *Phys. Rev. B*, 40:506–516, Jul 1989. [9](#)

[52] Thomas Schäfer, Nils Wentzell, Fedor Šimkovic, Yuan-Yao He, Cornelia Hille, Marcel Klett, Christian J. Eckhardt, Behnam Arzhang, Viktor Harkov, François-Marie Le Régent, Alfred

Kirsch, Yan Wang, Aaram J. Kim, Evgeny Kozik, Evgeny A. Stepanov, Anna Kauch, Sabine Andergassen, Philipp Hansmann, Daniel Rohe, Yuri M. Vilk, James P. F. LeBlanc, Shiwei Zhang, A.-M. S. Tremblay, Michel Ferrero, Olivier Parcollet, and Antoine Georges. Tracking the Footprints of Spin Fluctuations: A MultiMethod, MultiMessenger Study of the Two-Dimensional Hubbard Model. *Phys. Rev. X*, 11:011058, Mar 2021. [9](#)

[53] Mingpu Qin, Chia-Min Chung, Hao Shi, Ettore Vitali, Claudius Hubig, Ulrich Schollwöck, Steven R. White, and Shiwei Zhang. Absence of Superconductivity in the Pure Two-Dimensional Hubbard Model. *Phys. Rev. X*, 10:031016, Jul 2020. [9](#)

[54] Mingpu Qin, Thomas Schäfer, Sabine Andergassen, Philippe Corboz, and Emanuel Gull. The Hubbard model: A computational perspective. *Annual Review of Condensed Matter Physics*, 13(1):275–302, 2022. [9](#)

[55] Annabelle Bohrdt, Lukas Homeier, Christian Reinmoser, Eugene Demler, and Fabian Grusdt. Exploration of doped quantum magnets with ultracold atoms. *Annals of Physics*, 435:168651, 2021. [9](#)

[56] B. Coqblin and J. R. Schrieffer. Exchange interaction in alloys with cerium impurities. *Phys. Rev.*, 185:847–853, Sep 1969. [10](#), [28](#)

[57] S. Doniach. The Kondo lattice and weak antiferromagnetism. *Physica B+C*, 91:231–234, 1977. [10](#), [28](#)

[58] Y. Tokura, editor. *Colossal Magnetoresistive Oxides*. CRC Press, 2000. [10](#)

[59] Piers Coleman. *Heavy Fermions: Electrons at the Edge of Magnetism*, page 95–148. John Wiley & Sons, Ltd, 2007. [10](#)

[60] Yoshiro Takahashi. Quantum simulation of quantum many-body systems with ultracold two-electron atoms in an optical lattice. *Proceedings of the Japan Academy, Series B*, 98:141–160, 2022. [10](#), [26](#), [28](#)

[61] Miguel A Cazalilla and Ana Maria Rey. Ultracold Fermi gases with emergent $SU(N)$ symmetry. *Rep. Prog. Phys.*, 77:124401, 2014. [10](#), [26](#)

[62] Simon Stellmer, Florian Schreck, and Thomas C. Killian. *Degenerate Quantum Gases of Strontium*, chapter 1, pages 1–80. World Scientific, 2014. [10](#)

[63] Eduardo Ibarra-García-Padilla. *Quantum Simulation of the Hubbard Model: Higher Symmetry Fermions and New Architectures*. PhD thesis, Rice University, 2022. [11](#), [17](#)

[64] A Zee. *Group Theory in a Nutshell for Physicists*. Princeton University Press, 2016. [10](#)

[65] N Read and D M Newns. On the solution of the Coqblin-Schreiffer Hamiltonian by the large-N expansion technique. *J. Phys. C: Solid State Phys.*, 16:3273–3295, 1983. [11](#), [26](#)

[66] Ian Affleck. Large-N Limit of $SU(N)$ Quantum “Spin” Chains. *Phys. Rev. Lett.*, 54:966–969, 1985. [11](#), [26](#)

[67] Ian Affleck and J. Brad Marston. Large- n limit of the Heisenberg-Hubbard model: Implications for high- T_c superconductors. *Phys. Rev. B*, 37:3774–3777, 1988. [11](#), [26](#)

[68] N. E. Bickers. Review of techniques in the large-N expansion for dilute magnetic alloys. *Rev. Mod. Phys.*, 59:845–939, 1987. [11](#), [26](#)

[69] A. Auerbach. *Interacting Electrons and Quantum Magnetism*. Springer-Verlag New York, 1994. [11](#), [26](#)

[70] Y. Q. Li, Michael Ma, D. N. Shi, and F. C. Zhang. $SU(4)$ Theory for Spin Systems with Orbital Degeneracy. *Phys. Rev. Lett.*, 81:3527–3530, 1998. [12](#), [23](#)

[71] Y. Tokura. Orbital Physics in Transition-Metal Oxides. *Science*, 288:462–468, 2000. [12](#)

[72] Elbio Dagotto, Takashi Hotta, and Adriana Moreo. Colossal magnetoresistant materials: the key role of phase separation. *Physics reports*, 344(1-3):1–153, 2001. [12](#)

[73] M. Mancini, G. Pagano, G. Cappellini, L. Livi, M. Rider, J. Catani, C. Sias, P. Zoller, M. Inguscio, M. Dalmonte, and L. Fallani. Observation of chiral edge states with neutral fermions in synthetic Hall ribbons. *Science*, 349:1510–1513, 2015. [12](#), [19](#)

[74] Shintaro Taie, Rekishu Yamazaki, Seiji Sugawa, and Yoshiro Takahashi. An $SU(6)$ Mott insulator of an atomic Fermi gas realized by large-spin Pomeranchuk cooling. *Nat. Phys.*, 8(11):825–830,

Sep 2012. [13](#), [14](#), [15](#), [22](#)

[75] R Jördens, N Strohmaier, K Günter, H Moritz, and T. Esslinger. A mott insulator of fermionic atoms in an optical lattice. *Nature*, 455:204–207, 2008. [13](#)

[76] Tim Rom, Thorsten Best, Olaf Mandel, Artur Widera, Markus Greiner, Theodor W. Hänsch, and Immanuel Bloch. State selective production of molecules in optical lattices. *Phys. Rev. Lett.*, 93:073002, Aug 2004. [13](#)

[77] Seiji Sugawa, Kensuke Inaba, Shintaro Taie, Rekishu Yamazaki, Makoto Yamashita, and Yoshiro Takahashi. Interaction and filling-induced quantum phases of dual Mott insulators of bosons and fermions. *Nat. Phys.*, 7:642–648, 2011. [13](#)

[78] Christian Hofrichter, Luis Riegger, Francesco Scazza, Moritz Höfer, Diogo Rio Fernandes, Immanuel Bloch, and Simon Fölling. Direct probing of the Mott crossover in the $SU(N)$ Fermi-Hubbard model. *Phys. Rev. X*, 6:021030, Jun 2016. [14](#), [16](#), [17](#)

[79] Giulio Pasqualetti, Oscar Bettermann, Nelson Darkwah Oppong, Eduardo Ibarra-García-Padilla, Sohail Dasgupta, Richard T. Scalettar, Kaden R. A. Hazzard, Immanuel Bloch, and Simon Fölling. Equation of state and thermometry of the 2D $SU(N)$ Fermi-Hubbard model. *Phys. Rev. Lett.*, 132:083401, Feb 2024. [17](#), [18](#)

[80] Eduardo Ibarra-García-Padilla, Sohail Dasgupta, Hao-Tian Wei, Shintaro Taie, Yoshiro Takahashi, Richard T. Scalettar, and Kaden R. A. Hazzard. Universal thermodynamics of an $SU(N)$ Fermi-Hubbard model. *Phys. Rev. A*, 104:043316, Oct 2021. [17](#), [27](#)

[81] Eduardo Ibarra-García-Padilla, Chunhan Feng, Giulio Pasqualetti, Simon Fölling, Richard T. Scalettar, Ehsan Khatami, and Kaden R. A. Hazzard. Metal-insulator transition and magnetism of $SU(3)$ fermions in the square lattice. *Phys. Rev. A*, 108:053312, Nov 2023. [17](#), [27](#)

[82] S Nascimbène, N Navon, K J Jiang, F Chevy, and C Salomon. Exploring the thermodynamics of a universal fermi gas. *Nature*, 463:1057–1060, 2010. [17](#)

[83] Qi Zhou and Tin-Lun Ho. Universal thermometry for quantum simulation. *Phys. Rev. Lett.*, 106:225301, May 2011. [18](#)

[84] Thomas Hartke, Botond Oreg, Ningyuan Jia, and Martin Zwierlein. Doublon-hole correlations and fluctuation thermometry in a Fermi-Hubbard gas. *Phys. Rev. Lett.*, 125:113601, Sep 2020. [18](#)

[85] Daniele Tusi, Lorenzo Franchi, Lorenzo Francesco Livi, Karla Baumann, Daniel Benedicto Orenes, Lorenzo Del Re, Rafael Emilio Barfknecht, Tianwei Zhou, Massimo Inguscio, Giacomo Cappellini, Massimo Capone, Jacopo Catani, and Leonardo Fallani. Flavour-selective localization in interacting lattice fermions. *Nat. Phys.*, 18:1201–1205, 2022. [18](#), [19](#), [20](#)

[86] Hideki Ozawa, Shintaro Taie, Yosuke Takasu, and Yoshiro Takahashi. Antiferromagnetic spin correlation of $SU(N)$ Fermi gas in an optical superlattice. *Phys. Rev. Lett.*, 121:225303, Nov 2018. [21](#), [22](#), [23](#)

[87] D. Greif, T. Uehlinger, G. Jotzu, L. Tarruell, and T. Esslinger. Short-range quantum magnetism of ultracold fermions in an optical lattice. *Science*, 340(6138):1307–1310, may 2013. [21](#), [25](#)

[88] Shintaro Taie, Eduardo Ibarra-García-Padilla, Naoki Nishizawa, Yosuke Takasu, Yoshihito Kuno, Hao-Tian Wei, Richard T. Scalettar, Kaden R. A. Hazzard, and Yoshiro Takahashi. Observation of antiferromagnetic correlations in an ultracold $SU(N)$ Hubbard model. *Nat. Phys.*, 18:1356–1361, 2022. [21](#), [24](#), [25](#)

[89] Jakub Imriška, Mauro Iazzi, Lei Wang, Emanuel Gull, Daniel Greif, Thomas Uehlinger, Gregor Jotzu, Leticia Tarruell, Tilman Esslinger, and Matthias Troyer. Thermodynamics and magnetic properties of the anisotropic 3d Hubbard model. *Phys. Rev. Lett.*, 112:115301, Mar 2014. [25](#)

[90] Eduardo Ibarra-García-Padilla, Rick Mukherjee, Randall G. Hulet, Kaden R. A. Hazzard, Thereza Paiva, and Richard T. Scalettar. Thermodynamics and magnetism in the two-dimensional to three-dimensional crossover of the Hubbard model. *Phys. Rev. A*, 102:033340, Sep 2020. [25](#)

[91] Chunhan Feng, Eduardo Ibarra-García-Padilla, Kaden R. A. Hazzard, Richard Scalettar, Shiwei Zhang, and Ettore Vitali. Metal-insulator transition and quantum magnetism in the $SU(3)$

Fermi-Hubbard model. *Phys. Rev. Res.*, 5:043267, Dec 2023. [25](#), [27](#)

[92] Yuan-Yao He, Mingpu Qin, Hao Shi, Zhong-Yi Lu, and Shiwei Zhang. Finite-temperature auxiliary-field quantum Monte Carlo: Self-consistent constraint and systematic approach to low temperatures. *Phys. Rev. B*, 99:045108, Jan 2019. [25](#)

[93] Anton Mazurenko, Christie S. Chiu, Geoffrey Ji, Maxwell F. Parsons, Márton Kanász-Nagy, Richard Schmidt, Fabian Grusdt, Eugene Demler, Daniel Greif, and Markus Greiner. A cold-atom Fermi-Hubbard antiferromagnet. *Nature*, 545(7655):462–466, may 2017. [26](#)

[94] Carsten Honerkamp and Walter Hofstetter. Ultracold fermions and the $SU(N)$ Hubbard Model. *Phys. Rev. Lett.*, 92:170403, 2004. [27](#)

[95] Da Wang, Yi Li, Zi Cai, Zhichao Zhou, Yu Wang, and Congjun Wu. Competing orders in the 2D half-filled $SU(2N)$ Hubbard model through the pinning-field quantum Monte Carlo simulations. *Phys. Rev. Lett.*, 112(15), apr 2014. [27](#)

[96] Da Wang, Lei Wang, and Congjun Wu. Slater and Mott insulating states in the $SU(6)$ Hubbard model. *Phys. Rev. B*, 100:115155, Sep 2019. [27](#)

[97] Zhichao Zhou, Zi Cai, Congjun Wu, and Yu Wang. Quantum Monte Carlo simulations of thermodynamic properties of $SU(2N)$ ultracold fermions in optical lattices. *Phys. Rev. B*, 90(23), dec 2014. [27](#)

[98] Rajiv R. P. Singh and Jaan Oitmaa. Finite-temperature strong-coupling expansions for the $SU(N)$ Hubbard model. *Phys. Rev. A*, 105:033317, Mar 2022. [27](#)

[99] Zhichao Zhou, Congjun Wu, and Yu Wang. Mott transition in the π -flux $SU(4)$ Hubbard model on a square lattice. *Phys. Rev. B*, 97:195122, May 2018. [27](#)

[100] Han Xu, Yu Wang, Zhichao Zhou, and Congjun Wu. Mott insulating states of the anisotropic $SU(4)$ Dirac fermions. *Phys. Rev. B*, 109:125136, Mar 2024. [27](#)

[101] A. Golubeva, A. Sotnikov, A. Cichy, J. Kuneš, and W. Hofstetter. Breaking of $SU(4)$ symmetry and interplay between strongly correlated phases in the Hubbard model. *Phys. Rev. B*, 95:125108, Mar 2017. [27](#)

[102] Gang Chen, Kaden R. A. Hazzard, Ana Maria Rey, and Michael Hermele. Synthetic-gauge-field stabilization of the chiral-spin-liquid phase. *Phys. Rev. A*, 93:061601, Jun 2016. [27](#)

[103] Vladyslav Unukovych and Andrii Sotnikov. $SU(4)$ -symmetric Hubbard model at quarter filling: Insights from the dynamical mean-field approach. *Phys. Rev. B*, 104:245106, Dec 2021. [27](#)

[104] M A Cazalilla, A F Ho, and M Ueda. Ultracold gases of ytterbium: Ferromagnetism and Mott states in an $SU(6)$ Fermi system. *New J. Phys.*, 11:103033, 2009. [27](#)

[105] Thomas Botzung and Pierre Nataf. Exact diagonalization of $SU(N)$ Fermi-Hubbard models. *Phys. Rev. Lett.*, 132:153001, Apr 2024. [27](#), [28](#)

[106] Evgeny Kozik. Combinatorial summation of Feynman diagrams: Equation of state of the 2D $SU(N)$ Hubbard model. *arXiv:2309.13774*, 2024. [27](#)

[107] F. F. Assaad. Phase diagram of the half-filled two-dimensional $SU(N)$ Hubbard-Heisenberg model: A quantum Monte Carlo study. *Phys. Rev. B*, 71:075103, 2005. [27](#)

[108] Yunqing Ouyang and Xiao Yan Xu. Projection of infinite- U Hubbard model and algebraic sign structure. *Phys. Rev. B*, 104:L241104, Dec 2021. [27](#)

[109] Thomas Botzung and Pierre Nataf. Numerical observation of $SU(N)$ Nagaoka ferromagnetism. *Phys. Rev. B*, 109:235131, Jun 2024. [27](#)

[110] I Titvinidze, A Privitera, S-Y Chang, S Diehl, M A Baranov, A Daley, and W Hofstetter. Magnetism and domain formation in $SU(3)$ -symmetric multi-species Fermi mixtures. *New J. Phys.*, 13:035013, 2011. [27](#)

[111] Andrii Sotnikov and Walter Hofstetter. Magnetic ordering of three-component ultracold fermionic mixtures in optical lattices. *Phys. Rev. A*, 89:063601, Jun 2014. [27](#)

[112] Andrii Sotnikov. Critical entropies and magnetic-phase-diagram analysis of ultracold three-component fermionic mixtures in optical lattices. *Phys. Rev. A*, 92:023633, Aug 2015. [27](#)

[113] Salvatore R. Manmana, Kaden R. A. Hazzard, Gang Chen, Adrian E. Feiguin, and Ana Maria Rey. $SU(N)$ magnetism in chains of ultracold alkaline-earth-metal atoms: Mott transitions

and quantum correlations. *Phys. Rev. A*, 84:043601, Oct 2011. [27](#)

[114] Lars Bonnes, Kaden R. A. Hazzard, Salvatore R. Manmana, Ana Maria Rey, and Stefan Wessel. Adiabatic loading of one-dimensional $SU(N)$ alkaline-earth-atom fermions in optical lattices. *Phys. Rev. Lett.*, 109:205305, Nov 2012. [27](#)

[115] Roland Assaraf, Patrick Azaria, Michel Caffarel, and Philippe Lecheminant. Metal-insulator transition in the one-dimensional $SU(N)$ Hubbard model. *Phys. Rev. B*, 60(4):2299, 1999. [27](#)

[116] Shenglong Xu, Julio T. Barreiro, Yu Wang, and Congjun Wu. Interaction effects with varying N in $SU(N)$ symmetric fermion lattice systems. *Phys. Rev. Lett.*, 121:167205, Oct 2018. [27](#)

[117] A. Pérez-Romero, R. Franco, and J. Silva-Valencia. Phase diagram of the $SU(3)$ Fermi Hubbard model with next-neighbor interactions. *Euro Phys J B*, 94(11):229, nov 2021. [27](#)

[118] K Buchta, Ö Legeza, E Szirmai, and J Sólyom. Mott transition and dimerization in the one-dimensional $SU(N)$ Hubbard model. *Phys. Rev. B*, 75(15):155108, 2007. [27](#)

[119] Yasufumi Yamashita, Naokazu Shibata, and Kazuo Ueda. $SU(4)$ spin-orbit critical state in one dimension. *Phys. Rev. B*, 58(14):9114, 1998. [27](#)

[120] Mathias Mikkelsen and Ippei Danshita. Relation between the noise correlations and the spin structure factor for Mott-insulating states in $SU(N)$ Hubbard models. *Phys. Rev. A*, 107:043313, Apr 2023. [27](#)

[121] Rahul Hingorani, Jaan Oitmaa, and Rajiv R. P. Singh. Onset of charge incompressibility and Mott gaps in the honeycomb-lattice $SU(4)$ Hubbard model: Lessons for twisted bilayer graphene systems. *Phys. Rev. B*, 105:L241410, Jun 2022. [27](#)

[122] Zhichao Zhou, Da Wang, Zi Yang Meng, Yu Wang, and Congjun Wu. Mott insulating states and quantum phase transitions of correlated $SU(2N)$ Dirac fermions. *Phys. Rev. B*, 93:245157, Jun 2016. [27](#)

[123] Zhichao Zhou, Da Wang, Congjun Wu, and Yu Wang. Finite-temperature valence-bond-solid transitions and thermodynamic properties of interacting $SU(2N)$ Dirac fermions. *Phys. Rev. B*, 95:085128, Feb 2017. [27](#)

[124] Han Xu, Xiang Li, Zhichao Zhou, Xin Wang, Lei Wang, Congjun Wu, and Yu Wang. Trion states and quantum criticality of attractive $SU(3)$ Dirac fermions. *Phys. Rev. Res.*, 5:023180, Jun 2023. [27](#)

[125] Rajiv R. P. Singh and Jaan Oitmaa. Divergence of magnetic susceptibility in the $SU(N)$ Nagaoka-Thouless ferromagnet. *Phys. Rev. B*, 106:014424, Jul 2022. [27, 28](#)

[126] Mohsen Hafez-Torbat and Walter Hofstetter. Artificial $SU(3)$ spin-orbit coupling and exotic Mott insulators. *Phys. Rev. B*, 98:245131, Dec 2018. [27](#)

[127] Mohsen Hafez-Torbat and Walter Hofstetter. Competing charge and magnetic order in fermionic multicomponent systems. *Phys. Rev. B*, 100:035133, Jul 2019. [27](#)

[128] Mohsen Hafez-Torbat, Jun-Hui Zheng, Bernhard Irsigler, and Walter Hofstetter. Interaction-driven topological phase transitions in fermionic $SU(3)$ systems. *Phys. Rev. B*, 101:245159, Jun 2020. [27](#)

[129] Wenxing Nie, Deping Zhang, and Wei Zhang. Ferromagnetic ground state of the $SU(3)$ Hubbard model on the Lieb lattice. *Phys. Rev. A*, 96(5):053616, 2017. [27](#)

[130] Kaden R. A. Hazzard, Victor Gurarie, Michael Hermele, and Ana Maria Rey. High-temperature properties of fermionic alkaline-earth-metal atoms in optical lattices. *Phys. Rev. A*, 85:041604, 2012. [27](#)

[131] Seung-Sup B. Lee, Jan von Delft, and Andreas Weichselbaum. Filling-driven Mott transition in $SU(N)$ Hubbard models. *Phys. Rev. B*, 97:165143, Apr 2018. [27](#)

[132] Hiromasa Yanatori and Akihisa Koga. Finite-temperature phase transitions in the $SU(N)$ Hubbard model. *Phys. Rev. B*, 94:041110, Jul 2016. [27](#)

[133] Tamás A. Tóth, Andreas M. Läuchli, Frédéric Mila, and Karlo Penc. Three-sublattice ordering of the $SU(3)$ Heisenberg model of three-flavor fermions on the square and cubic lattices. *Phys. Rev. Lett.*, 105:265301, 2010. [26, 27](#)

[134] Bela Bauer, Philippe Corboz, Andreas M. Läuchli, Laura Messio, Karlo Penc, Matthias Troyer,

and Frédéric Mila. Three-sublattice order in the $SU(3)$ Heisenberg model on the square and triangular lattice. *Phys. Rev. B*, 85:125116, 2012. [26](#), [27](#)

[135] Philippe Corboz, Andreas M. Läuchli, Karlo Penc, Matthias Troyer, and Frédéric Mila. Simultaneous dimerization and $SU(4)$ symmetry breaking of 4-color fermions on the square lattice. *Phys. Rev. Lett.*, 107:215301, 2011. [27](#)

[136] Michael Hermele, Victor Gurarie, and Ana Maria Rey. Mott insulators of ultracold fermionic alkaline earth atoms: Underconstrained magnetism and chiral spin liquid. *Phys. Rev. Lett.*, 103:135301, Sep 2009. [27](#)

[137] Pierre Nataf and Frédéric Mila. Exact Diagonalization of Heisenberg $SU(N)$ Models. *Phys. Rev. Lett.*, 113:127204, 2014. [27](#)

[138] Michael Hermele and Victor Gurarie. Topological liquids and valence cluster states in two-dimensional $SU(N)$ magnets. *Phys. Rev. B*, 84:174441, Nov 2011. [26](#), [27](#)

[139] Laura Messio and Frédéric Mila. Entropy dependence of correlations in one-dimensional $SU(N)$ antiferromagnets. *Phys. Rev. Lett.*, 109:205306, Nov 2012. [27](#)

[140] Christian Romen and Andreas M. Läuchli. Structure of spin correlations in high-temperature $SU(N)$ quantum magnets. *Phys. Rev. Research*, 2:043009, Oct 2020. [27](#)

[141] L. Herviou, S. Capponi, and P. Lecheminant. Even-odd effects in the $J_1-J_2su(n)$ Heisenberg spin chain. *Phys. Rev. B*, 107:205135, May 2023. [27](#)

[142] W. M. H. Natori, R. Nutakki, R. G. Pereira, and E. C. Andrade. $SU(4)$ Heisenberg model on the honeycomb lattice with exchange-frustrated perturbations: Implications for twistronics and Mott insulators. *Phys. Rev. B*, 100:205131, Nov 2019. [27](#)

[143] Daisuke Yamamoto, Chihiro Suzuki, Giacomo Marmorini, Sho Okazaki, and Nobuo Furukawa. Quantum and thermal phase transitions of the triangular $SU(3)$ Heisenberg model under magnetic fields. *Phys. Rev. Lett.*, 125:057204, Jul 2020. [26](#), [27](#)

[144] Xu-Ping Yao, Yonghao Gao, and Gang Chen. Topological chiral spin liquids and competing states in triangular lattice $SU(N)$ Mott insulators. *Phys. Rev. Research*, 3:023138, May 2021. [27](#)

[145] Henning Schrömer, Fabian Grusdt, Ulrich Schollwöck, Kaden R. A. Hazzard, and Annabelle Bohrdt. Sub-dimensional magnetic polarons in the one-hole doped $SU(3)$ t-J model. *arXiv:2312.14137*, 2023. [27](#)

[146] Jia-Cheng He, Jun-Hao Zhang, and Jie Lou and Yan Chen. Six-component pairing instability in the $SU(4)$ $t - J$ chain. *arXiv:2311.06601*, 2024. [27](#)

[147] Gang V. Chen and Congjun Wu. Multiflavor Mott insulators in quantum materials and ultracold atoms. *npj Quantum Mater.*, 9:1, 2024. [26](#)

[148] Philippe Corboz, Miklós Lajkó, Karlo Penc, Frédéric Mila, and Andreas M Läuchli. Competing states in the $su(3)$ heisenberg model on the honeycomb lattice: Plaquette valence-bond crystal versus dimerized color-ordered state. *Physical Review B—Condensed Matter and Materials Physics*, 87(19):195113, 2013. [26](#)

[149] Hui-Hai Zhao, Cenke Xu, QN Chen, ZC Wei, MP Qin, GM Zhang, and T Xiang. Plaquette order and deconfined quantum critical point in the spin-1 bilinear-biquadratic heisenberg model on the honeycomb lattice. *Phys. Rev. B*, 85(13):134416, 2012. [26](#)

[150] Yu-Wen Lee and Min-Fong Yang. Spontaneous dimerization in the spin-1 bilinear-biquadratic heisenberg model on a honeycomb lattice. *Phys. Rev. B*, 85(10):100402(R), 2012. [26](#)

[151] Ryuta Yamamoto, Jun Kobayashi, Takuma Kuno, Kohei Kato, and Yoshiro Takahashi. An ytterbium quantum gas microscope with narrow-line laser cooling. *New J. Phys.*, 18(2):023016, feb 2016. [28](#)

[152] Daichi Okuno, Yoshiki Amano, Katsunari Enomoto, Nobuyuki Takei, and Yoshiro Takahashi. Schemes for nondestructive quantum gas microscopy of single atoms in an optical lattice. *New J. Phys.*, 22(1):013041, jan 2020. [28](#)

[153] Sandra Buob, Jonatan Höschele, Vasiliy Makhlov, Antonio Rubio-Abadal, and Leticia Tarruell. A strontium quantum-gas microscope. *PRX Quantum*, 5:020316, Apr 2024. [28](#)

[154] Lin Su, Alexander Douglas, Michal Szurek, Anne H. Hébert, Aaron Krahn, Robin Groth, Gregory A. Phelps, Ognjen Marković, and Markus Greiner. Fast single atom imaging in optical lattice arrays. *arXiv:2404.09978*, 2024. [28](#)

[155] Aaron Merlin Müller, Miklós Lajkó, Florian Schreck, Frédéric Mila, and Jiří Minář. State selective cooling of $SU(N)$ Fermi gases. *Phys. Rev. A*, 104:013304, Jul 2021. [28](#)

[156] Daisuke Yamamoto and Katsuhiro Morita. Engineering of a low-entropy quantum simulator for strongly correlated electrons using cold atoms with $SU(N)$ -symmetric interactions. *Phys. Rev. Lett.*, 132:213401, May 2024. [28](#)

[157] Christie S. Chiu, Geoffrey Ji, Annabelle Bohrdt, Muqing Xu, Michael Knap, Eugene Demler, Fabian Grusdt, Markus Greiner, and Daniel Greif. String patterns in the doped Hubbard model. *Science*, 365(6450):251–256, 2019. [28](#)

[158] Joannis Koepsell, Dominik Bourgund, Pimonpan Sompet, Sarah Hirthe, Annabelle Bohrdt, Yao Wang, Fabian Grusdt, Eugene Demler, Guillaume Salomon, Christian Gross, and Immanuel Bloch. Microscopic evolution of doped Mott insulators from polaronic metal to Fermi liquid. *Science*, 374(6563):82–86, 2021. [28](#)

[159] Shan-Yue Wang, Da Wang, and Qiang-Hua Wang. Transition from band insulator to Mott insulator and formation of local moment in the half-filled ionic $SU(N)$ Hubbard model. *Phys. Rev. B*, 106:245113, Dec 2022. [28](#)

[160] Matteo Ferrareto, Andrea Richaud, Lorenzo Del Re, Leonardo Fallani, and Massimo Capone. Enhancement of chiral edge currents in $(d+1)$ -dimensional atomic Mott-band hybrid insulators. *SciPost Phys.*, 14:048, 2023. [28](#)

[161] Peter T. Brown, Debayan Mitra, Elmer Guardado-Sánchez, Reza Nourafkan, Alexis Reymbaut, Charles-David Hébert, Simon Bergeron, A.-M. S. Tremblay, Jure Kokalj, David A. Huse, Peter Schauß, and Waseem S. Bakr. Bad metallic transport in a cold atom Fermi-Hubbard system. *Science*, 363(6425):379–382, dec 2018. [28](#)

[162] Matthew A. Nichols, Lawrence W. Cheuk, Melih Okan, Thomas R. Hartke, Enrique Mendez, T. Senthil, Ehsan Khatami, Hao Zhang, and Martin W. Zwierlein. Spin transport in a Mott insulator of ultracold fermions. *Science*, 363(6425):383–387, 2018. [28](#)

[163] Miklós Antal Werner, Cătălin Pașcu Moca, Márton Kormos, Örs Legeza, Balázs Dóra, and Gergely Zaránd. Spectroscopic evidence for engineered hadronic bound state formation in repulsive fermionic $SU(N)$ Hubbard systems. *Phys. Rev. Res.*, 5:043020, Oct 2023. [28](#)

[164] Dávid Jakab and Zoltán Zimborás. Quantum phases of collective $SU(3)$ spin systems with bipartite symmetry. *Phys. Rev. B*, 103(21):214448, 2021. [28](#)

[165] Federica Maria Surace, Pierre Fromholz, Francesco Scazza, and Marcello Dalmonte. Scalable, ab initio protocol for quantum simulating $SU(N) \times U(1)$ lattice gauge theories. *Quantum*, 8:1359, 2024. [28](#)

[166] Andrii Sotnikov, Nelson Darkwah Oppong, Yeimer Zambrano, and Agnieszka Cichy. Orbital ordering of ultracold alkaline-earth atoms in optical lattices. *Phys. Rev. Res.*, 2:023188, May 2020. [28](#)

[167] Kensuke Tamura and Hoshio Katsura. Flat-band ferromagnetism in the $SU(N)$ Hubbard and Kondo lattice models. *Journal of Physics A: Mathematical and Theoretical*, 56(39):395202, sep 2023. [28](#)

[168] Keisuke Totsuka. Ferromagnetism in the $SU(N)$ Kondo lattice model: $SU(N)$ double exchange and supersymmetry. *Phys. Rev. A*, 107:033317, Mar 2023. [28](#)

[169] Miklós Antal Werner, Cătălin Pașcu Moca, Örs Legeza, and Gergely Zaránd. Quantum quench and charge oscillations in the $SU(3)$ Hubbard model: A test of time evolving block decimation with general non-abelian symmetries. *Phys. Rev. B*, 102(15):155108, 2020. [28](#)

[170] Yicheng Zhang, Lev Vidmar, and Marcos Rigol. Quantum dynamics of impenetrable $SU(N)$ fermions in one-dimensional lattices. *Phys. Rev. A*, 99(6):063605, 2019. [28](#)

[171] Gyorgy Fehér and Balázs Pozsgay. Generalized gibbs ensemble and string-charge relations in nested bethe ansatz. *SciPost Physics*, 8(3):034, 2020. [28](#)

- [172] Mikhail Mamaev, Thomas Bilitewski, Bhuvanesh Sundar, and Ana Maria Rey. Resonant dynamics of strongly interacting $SU(N)$ fermionic atoms in a synthetic flux ladder. *PRX Quantum*, 3(3):030328, 2022. [28](#)
- [173] Enej Ilievski, Jacopo De Nardis, Bram Wouters, J-S Caux, Fabian HL Essler, and Tomaz Prosen. Complete generalized gibbs ensembles in an interacting theory. *Phys. Rev. Lett.*, 115(15):157201, 2015. [28](#)
- [174] Paola Ruggiero, Pasquale Calabrese, Benjamin Doyon, and Jérôme Dubail. Quantum generalized hydrodynamics. *Phys. Rev. Lett.*, 124(14):140603, 2020. [28](#)
- [175] Markus Heyl. Dynamical quantum phase transitions: a review. *Reports on Progress in Physics*, 81(5):054001, 2018. [29](#)
- [176] Aleksandr N Mikheev, Ido Siovitz, and Thomas Gasenzer. Universal dynamics and non-thermal fixed points in quantum fluids far from equilibrium. *The European Physical Journal Special Topics*, 232(20):3393–3415, 2023. [29](#)
- [177] Bijit Mukherjee, Jeremy M. Hutson, and Kaden R. A. Hazzard. $SU(N)$ magnetism with ultracold molecules. *arXiv:2404.15957v1*, 2024. [29](#)
- [178] Koki Chinzei and Tatsuhiko N Ikeda. Time crystals protected by Floquet dynamical symmetry in Hubbard models. *Phys. Rev. Lett.*, 125(6):060601, 2020. [29](#)